

Fast and Reliable Gradients for Deformables Across Frictional Contact Regimes

ZIQU ZENG, National University of Singapore, Singapore and Prana Lab, USA

GANG YANG, National University of Singapore, Singapore

ZHENHAO HUANG, National University of Singapore, Singapore

YULIN LI, National University of Singapore, Singapore

JASON PHO, Prana Lab, USA

SIYUAN LUO*, Prana Lab, USA

FAN SHI†, National University of Singapore, Singapore

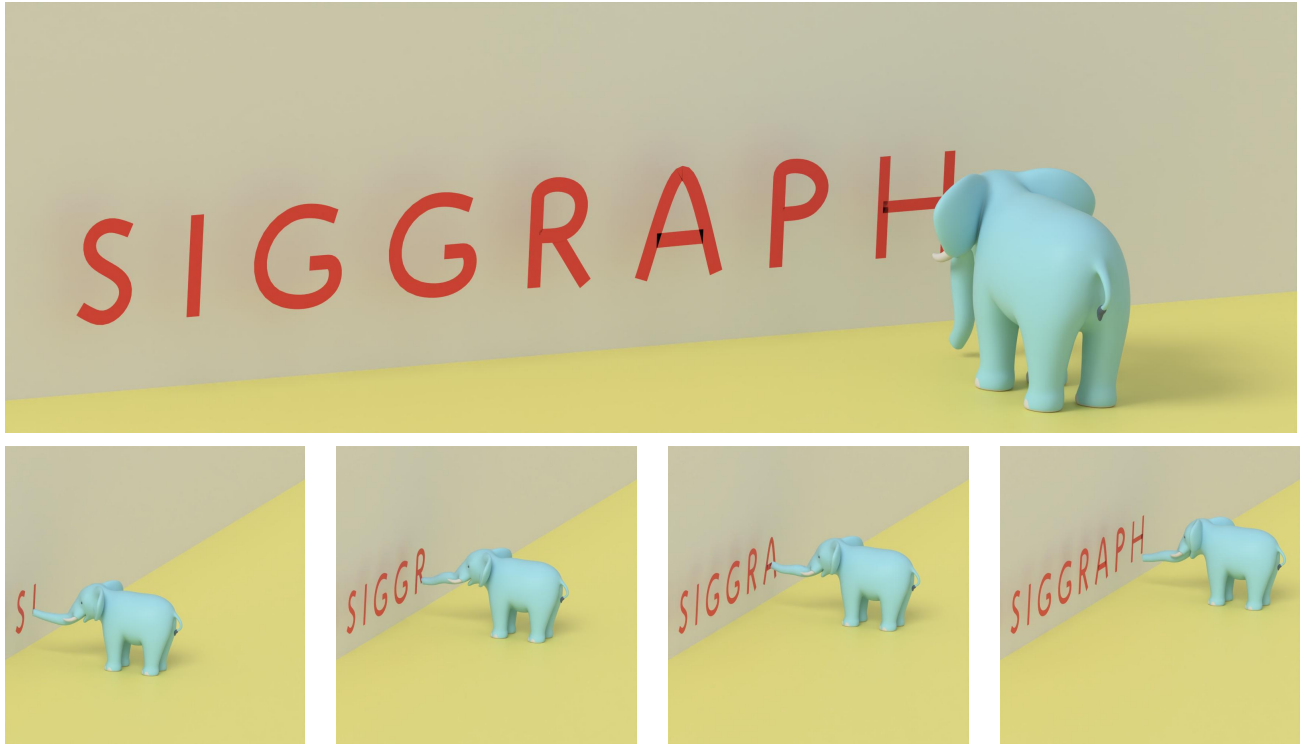


Fig. 1. **Taming the Elephant in the Room:** We simulate a soft, cable-driven elephant trunk writing "SIGGRAPH" on a wall. Our differentiable physics engine optimizes strongly coupled elastic dynamics involving frictional contact and state-based controls. Using direct gradient descent from a rest state, we optimize the four-cable actuation for each letter in under one hour on a single NVIDIA RTX 5090 GPU. (see Fig. 12)

Differentiable simulation establishes the mathematical foundation for solving challenging inverse problems in computer graphics and robotics, such as physical system identification and inverse dynamics control. However, rigor in frictional contact remains the "elephant in the room." Current frameworks

* Corresponding author.

† Corresponding author.

Authors' Contact Information: Ziqu Zeng, National University of Singapore, Singapore and Prana Lab, USA, zzeng@nus.edu.sg; Gang Yang, National University of Singapore, Singapore, ygang@u.nus.edu; Zhenhao Huang, National University of Singapore, Singapore, huangzhenhao@u.nus.edu; Yulin Li, National University of Singapore, Singapore, yline@nus.edu.sg; Jason Pho, Prana Lab, USA, pho@pranalab.ai; Siyuan Luo, Prana Lab, USA, sy.luo@nus.edu.sg; Fan Shi, National University of Singapore, Singapore, fan.shi@nus.edu.sg.

often avoid contact singularities via non-Markovian position approximations or heuristic gradients. This lack of mathematical consistency distorts gradients, causing optimization stagnation or failure in complex frictional contact and large-deformation scenarios. We introduce our unified fully GPU-accelerated differentiable simulator, which establishes a rigorous theoretical paradigm through: **Long-Horizon Consistency:** enforcing strict Markovian dynamics on a coupled position-velocity manifold to prevent gradient collapse; **Unified Contact Stability:** employing a mass-aligned preconditioner and soft Fischer–Burmeister operator for smooth frictional optimization; **Robust Material Identification:** resolving FEM singularities via a derived "Within-block Commutation" condition. Our experiments demonstrate our solver efficacy in bridging the Sim-to-Real gap, delivering

precise, low-noise gradients in contact-rich tasks like dexterous manipulation and cloth folding. By mitigating the gradient instability issues common in conventional approaches, our framework significantly enhances the fidelity of physical system identification and control.

CCS Concepts: • **Computing methodologies** → **Physical simulation**; **Real-time simulation**; *Parallel algorithms*.

Additional Key Words and Phrases: Physics-based simulation, Differentiable simulation, Gradient-based Optimization, GPU parallelization

1 Introduction

Physical simulation in computer graphics has primarily focused on the forward problem: generating visually plausible motion trajectories given physical parameters, initial states, and external conditions. However, with the deep convergence of robotics and artificial intelligence, we are witnessing a paradigm shift from "visual synthesis" to "physical grounding". In this case, the inverse problem has emerged as a central challenge: Can we infer material properties by observing object motion? Or can we directly optimize control forces to achieve complex interaction goals? Consequently, differentiable simulation has emerged as the critical bridge spanning this gap. By formulating the physics simulator as a fully differentiable computational graph, we enable the backpropagation of gradients from high-level task objectives—such as "folding a cloth" or "grasping a cup"—directly to low-level physical parameters or control inputs. This end-to-end optimization capability opens up compelling prospects for system identification in soft materials and inverse dynamics control in manipulation [17, 23].

A fundamental challenge in differentiable simulation is the trade-off between physical fidelity and gradient stability, particularly when handling complex contact and large deformations. To prioritize visual stability and prevent artifacts like interpenetration, many frameworks resort to numerical heuristics within their solvers, such as aggressive constraint relaxation or iterative position-level projections [3, 20]. While effective for forward simulation, these techniques introduce a critical flaw for gradient-based optimization. The state update at each timestep becomes dependent not only on the physical state (position, velocity) but also on solver-internal parameters like iteration counts and ad-hoc correction histories [11]. This entanglement breaks the direct, physical cause-and-effect relationship that underpins the system's formal dynamics. As a result, the computed gradients become sensitive to numerical artifacts rather than true physical derivatives, leading to a rugged optimization landscape [33, 34]. Gradients can be noisy, vanish unexpectedly, or explode during critical contact events, causing optimization to stagnate and fail in precisely the contact-rich robotics tasks where it is most needed [24, 26].

To bridge this gap, we introduce our unified differentiable simulation framework designed for high-fidelity physical inference. Our philosophy emphasizes mathematical rigor as the primary driver of computational robustness. By integrating contact, deformation, and time integration into a unified framework, we ensure high physical fidelity and inherent smoothness, paving the way for more effective optimization. In summary, our contributions are listed as follows:

- We introduce a smoothed NCP-based formulation that yields well-defined and reliable gradients across non-smooth transitions, including contact and separation as well as static and kinetic friction.
- We ensure long-horizon consistency between the physical model, the forward simulation, and the backward differentiation, avoiding gradient degradation commonly caused by history-dependent heuristic approximations.
- We derive a unified adjoint formulation that exploits intrinsic structure to unlock scalable solvers algorithmically aligned with modern GPU architectures.

2 Related Work

2.1 Dynamics

The core of differentiable simulation lies in computing gradients of physical processes, which enables gradient-based optimization methods to be directly applied to tasks such as system identification and control policy learning [24]. Current gradient calculation methods are primarily categorized into Automatic Differentiation (AD) and Analytical Differentiation.

Automatic differentiation utilizes the chain rule to propagate derivatives at the level of basic operations [2] and is widely used in simulation frameworks based on PyTorch, JAX [27, 29], or high-performance JIT compilers like Warp [18]. However, as simulation complexity increases, AD can incur significant computational and memory overhead [12]. In contrast, analytical differentiation, by deriving explicit expressions for gradients, typically offers higher computational efficiency and accuracy [30], particularly when dealing with discontinuous dynamics such as contact [8]. Notably, the Adjoint Method obtains adjoint vectors by solving a linear system, avoiding expensive differential calculations for the entire state trajectory, thereby significantly reducing computational costs [28].

In terms of dynamics models, Newtonian Dynamics is the most fundamental form in rigid body simulation, describing the relationship between force and acceleration directly through equations of motion [5]. For soft and deformable bodies, Projective Dynamics (PD) transforms the dynamics problem into an energy minimization problem, providing a fast and robust implicit integration scheme [3]. DiffPD further extends PD into a differentiable form, enabling it to be integrated into gradient-based learning pipelines [6]. Building on this, DiffCloth incorporates dry frictional contact directly into the Projective Dynamics framework, utilizing a specialized solver to handle complementarity conditions for efficient cloth manipulation tasks. [15, 34] Furthermore, Extended Position-Based Dynamics (XPBD), as a position-based constraint solver, satisfies physical constraints by directly updating particle positions. It not only demonstrates excellent stability when simulating complex systems coupled with rigid contacts and internal constraints [20], but recent research has also demonstrated the feasibility of deriving its analytical gradients [31].

2.2 Contact

Modeling contact is the most challenging aspect of differentiable simulation, primarily due to the gradient discontinuity caused by the binary nature of contact states (contact vs. non-contact) [24].

Existing contact solvers and their differentiation schemes generally fall into three categories: Complementarity-based methods, Compliant/Penalty models, and Position-based methods.

Complementarity-based methods model contact as a Nonlinear Complementarity Problem (NCP) or its linearized approximation (LCP) to strictly enforce non-penetration [5, 30]. These problems are typically solved using the Projected Gauss-Seidel (PGS) method [9]. To obtain gradients, researchers often apply implicit differentiation to the Karush-Kuhn-Tucker (KKT) conditions [14]. However, the truncation of PGS iterations may result in complementarity constraints not being strictly satisfied, leading to inaccurate gradients from implicit differentiation. To address this, approaches like the reverse PGS method have been proposed to compute gradients using the adjoint method, avoiding the overhead of automatic differentiation while improving accuracy [28]. A related class of impulse-based methods, while easier to differentiate, suffers from inaccurate gradients at collision points due to naive time discretization [12]. To mitigate this, Continuous time of-Impact (TOI) methods have been introduced to compute the precise time of collisions, yielding significantly more accurate gradients for contact-rich tasks [36, 37].

To avoid the undefined gradients associated with hard contacts, Compliant Models or penalty methods adopt a "soft" contact strategy, allowing slight penetration and generating repulsive forces [6, 8]. Common practices involve using piecewise linear functions (e.g., ReLU) or nonlinear spring-damper models to approximate normal and frictional forces [13]. Although this relaxation makes contact forces continuously differentiable [10], simple linearized models yield zero gradients in inactive contact regions, potentially hindering the optimizer from discovering new contact modes. Recent works address this by introducing Leaky ReLU-like mechanisms to provide non-zero gradients even when contacts are inactive [32], or by using smoother quadratic approximations.

Furthermore, Position-based methods satisfy non-penetration constraints by iteratively correcting positions. While standard XPBD is stable, deriving its gradients analytically has only recently been explored [31]. Alternatively, optimization-based approaches formulate contact resolution as a convex optimization problem—specifically Quadratic Programs (QP) or Quadratically Constrained Quadratic Programs (QCQP)—and extract gradients via implicit differentiation of optimality conditions [14, 22]. To accelerate the computation of these gradients, specialized linear algebra techniques, such as QR decomposition, are employed to efficiently solve the resulting linear systems [16].

3 Background

This section reviews the forward simulation of deformable multi-body dynamics with contact used in our simulator, following [35]. Each time step is expressed as a *coupled residual system* over the next state, auxiliary constraint variables, external controls, and physical parameters, see Equation (6), which will later serve as the entry point for analytic gradients in Section 4. This residual-centric view is deliberate: it allows us to differentiate the *converged* solution via implicit differentiation, rather than unrolling solver iterations. Moreover, we adopt a unified NCP residual (via smoothed Fischer–Burmeister) so that contact is treated consistently in both

the forward pass and the backward Jacobian assembly. Finally, we introduce projective local states for internal elasticity, which makes the resulting Jacobian structure modular and amenable to efficient assembly in Section 4.

3.1 Deformable Multi-body Dynamics

Following [21], given current positions $\bar{\mathbf{q}}$ and velocities $\bar{\mathbf{v}}$ at time t , the implicit Euler time integration solves the optimization problem below to obtain new positions \mathbf{q} at time $t + h$:

$$\mathbf{q} = \arg \min_{\mathbf{q}'} \left(\frac{1}{2h^2} \|\mathbf{M}^{\frac{1}{2}}(\mathbf{q}' - \bar{\mathbf{q}})\|_F^2 + \sum_i \psi_i(\mathbf{q}') \right), \quad (1)$$

where \mathbf{M} denotes mass matrix, $\tilde{\mathbf{q}} = \bar{\mathbf{q}} + h\bar{\mathbf{v}} + h^2\mathbf{M}^{-1}\mathbf{f}_{\text{ext}}$ is the predicted state with external force \mathbf{f}_{ext} when elasticity is absent, and ψ signifies the elastic energy for finite elements.

The typical Lagrange multiplier method [19] then incorporates contact constraints into the dynamic system by treating contact forces $\boldsymbol{\lambda}$ as the Lagrange multipliers. Differentiating Equation (1) under the contact constraints yields:

$$\mathbf{M}(\mathbf{q} - \bar{\mathbf{q}}) - h^2\mathbf{f}_{\text{int}}(\mathbf{q}) - h^2 \sum_{j \in \mathcal{L}} \mathbf{H}_j^\top \boldsymbol{\lambda} = \mathbf{0} \quad (2a)$$

$$\forall j \in \mathcal{L}, \quad \boldsymbol{\phi}_j(\mathbf{q}, \boldsymbol{\lambda}) = \mathbf{0}, \quad (2b)$$

where \mathbf{f}_{int} denotes the implicit internal forces derived from $\psi(\mathbf{q})$, and \mathcal{L} represents the indices for Lagrangian constraints which are categorized into binding pairs $\mathcal{B} \subseteq \mathcal{L}$ and non-interpenetration pairs $\mathcal{C} \subseteq \mathcal{L}$. The contact Jacobian matrix \mathbf{H} maps the mechanical state to the contact space, and $\boldsymbol{\phi}(\mathbf{q}, \boldsymbol{\lambda})$ represents the bilateral condition for \mathcal{B} and Signorini-Coulomb condition for \mathcal{C} respectively. Equation (2) provides a unified residual form for one implicit time step. In the remainder of this section, we specify the constraint residuals $\boldsymbol{\phi}_j$ for (i) bilateral binding constraint and (ii) unilateral frictional contact, and we describe the projective formulation of internal forces that works for general elastic model.

3.2 Contact Constraints

We consider two categories of constraints in Equation (2): bilateral binding constraints, and unilateral non-interpenetration constraints with friction. Both are written as residual equations to enable a unified assembly into Equation (6).

3.2.1 Bilateral Binding. Such constraints arise in joint connections and other prescribed attachments (e.g., needle constraints [1] and cable constraints [4]). For each $b \in \mathcal{B}$, we define the constraint displacement $\boldsymbol{\delta}_b \in \mathbb{R}^3$ and the corresponding residual $\boldsymbol{\phi}_b$ via a linear spring model with stiffness E_b and rest displacement \mathbf{d}_b :

$$\boldsymbol{\delta}_b := \mathbf{H}_b \mathbf{q} - \mathbf{d}_b \quad (3a)$$

$$\boldsymbol{\phi}_b := \boldsymbol{\delta}_b + E_b \boldsymbol{\lambda}_b. \quad (3b)$$

3.2.2 Non-interpenetration and Frictional Contact. These constraints, usually with friction, are defined by collision detection and linearized along the contact normal and tangential directions. We refer readers to [7] for background on generating robust contact frames. Given a contact normal $\mathbf{n}_c \in \mathbb{R}^3$, the constraint displacement

$\delta_c \in \mathbb{R}^3$ is decomposed into a normal gap $\delta_n \in \mathbb{R}$ and a tangential component $\delta_f \in \mathbb{R}^2$, with $\mathbf{H}_c^\top = [\mathbf{H}_n^\top, \mathbf{H}_f^\top]$.

The normal force λ_n and friction force λ_f , together with δ_n and δ_f , satisfy complementarity conditions. To express these conditions as residual equations compatible with Equation (2), we adopt an NCP-function formulation and use the Fischer–Burmeister function $\phi_{\text{FB}}(x, y) := x + y - \sqrt{x^2 + y^2}$ throughout both forward simulation and backward differentiation (for more detailed explanation, please refer to [35]):

$$\delta_c = \begin{bmatrix} \delta_n \\ \delta_f \end{bmatrix} := \begin{bmatrix} \mathbf{H}_n \mathbf{q} - d_n \\ h \mathbf{H}_f \mathbf{v} - \mathbf{d}_f \end{bmatrix} = \begin{bmatrix} \mathbf{H}_n \mathbf{q} - d_n \\ \mathbf{H}_f (\mathbf{q} - \bar{\mathbf{q}}) - \mathbf{d}_f \end{bmatrix} \quad (4a)$$

$$\phi_c = \begin{bmatrix} \phi_n \\ \phi_f \\ \phi_{\parallel} \end{bmatrix} := \begin{bmatrix} \phi_{\text{FB}}(\delta_n, \lambda_n) \\ \phi_{\text{FB}}(\|\delta_f\|, \mu \lambda_n - \|\lambda_f\|) \\ \|\lambda_f\| \delta_f + \|\delta_f\| \lambda_f \end{bmatrix}, \quad (4b)$$

The compact form of δ_c highlights an important fact that will be repeatedly used later: normal and tangential components depend on the next-step state in different ways (via \mathbf{q} and \mathbf{v} , respectively), which enables a structured treatment of frictional contact in our unified residual system.

3.3 Projective Internal Force

We model elastic internal forces via local-global solvers [3, 25]. For each local elastic constraint, we introduce a projective state \mathbf{p}_i as the solution of a proximal-style local minimization: a quadratic penalty pulls \mathbf{p}_i towards current configuration, while the potential $\zeta_i(\cdot, \xi_i)$ encodes the desired constitutive manifold through its minimizers:

$$\mathbf{p}_i = \arg \min_{\mathbf{p}_i} \left(\frac{w_i}{2} \|\mathbf{p}_i' - \mathbf{G}_i \mathbf{q}\|_F^2 + \zeta_i(\mathbf{p}_i', \xi_i) \right) \quad (5a)$$

$$\Phi_i = \frac{w_i}{2} \|\mathbf{p}_i - \mathbf{G}_i \mathbf{q}\|_F^2 + \zeta_i(\mathbf{p}_i, \xi_i) \quad (5b)$$

$$\mathbf{f}_{\text{int}} = -\sum_i \nabla_{\mathbf{q}} \Phi_i = -\sum_i w_i \mathbf{G}_i^\top (\mathbf{G}_i \mathbf{q} - \mathbf{p}_i) \quad (5c)$$

where w_i is the (nonnegative) stiffness weight associated with the i -th local constraint.

Integrating Equations (3)–(5) into Equation (2) and concatenating all contacts of the same category, the complete Deformable Multi-body Dynamics becomes:

$$\overbrace{(\mathbf{M} + h^2 \sum_i w_i \mathbf{G}_i^\top \mathbf{G}_i)}^{\mathbf{A}} \mathbf{q} - \overbrace{(\mathbf{M} \bar{\mathbf{q}} + h^2 \sum_i w_i \mathbf{G}_i^\top \mathbf{p}_i)}^{\mathbf{b}} \quad (6a)$$

$$\begin{aligned} -h^2 \mathbf{H}_b^\top \lambda_b - h^2 \mathbf{H}_c^\top \lambda_c &= \mathbf{0} \\ \mathbf{H}_b \mathbf{q} - \mathbf{d}_b + E_b \lambda_b &= \mathbf{0} \end{aligned} \quad (6b)$$

$$\phi_{\text{FB}}(\delta_n, \lambda_n) = \mathbf{0} \quad (6c)$$

$$\phi_{\text{FB}}(\|\delta_f\|, \mu \lambda_n - \|\lambda_f\|) = \mathbf{0} \quad (6d)$$

$$\|\lambda_f\| \delta_f + \|\delta_f\| \lambda_f = \mathbf{0} \quad (6e)$$

$$w_i (\mathbf{p}_i - \mathbf{G}_i \mathbf{q}) + \nabla_{\mathbf{p}_i} \zeta_i(\mathbf{p}_i, \xi_i) = \mathbf{0}. \quad (6f)$$

Equation (6) defines one forward time step of our simulator. In Section 4, we differentiate this coupled system implicitly and introduce an adjoint formulation to obtain gradients with respect to states and physical parameters. Throughout the paper, ξ_i denotes local model parameters associated with the i -th projective energy (e.g., Young’s modulus and Poisson’s ratio), w_i is its stiffness weight, E_b

controls the compliance of binding constraints, and μ is the friction coefficient used in the NCP contact model.

While the efficiency and accuracy of such a forward system has been proven in [35], computing its gradient remains highly challenging, particularly due to the non-smoothness between contact and friction regimes, as well as strong non-linearity in local projections. In the next section, we present an analytic differentiation method for Equation (6). We begin by deriving the generic adjoint form induced by forward dynamics (Section 4.1). We then detail the Jacobian matrices contributed by frictional contact constraints (Section 4.2) and by the local projective dynamics (Section 4.3). Finally, we discuss practical strategies for solving the resulting adjoint linear system efficiently (Section 4.4).

4 Method

4.1 Generic Adjoint Form

Within one implicit time step, the kinematic relation $\mathbf{v} = \frac{1}{h}(\mathbf{q} - \bar{\mathbf{q}})$ makes \mathbf{v} an explicit function of \mathbf{q} and $\bar{\mathbf{q}}$, so that $\frac{\partial \mathbf{v}}{\partial \mathbf{q}} = \frac{1}{h}$ and $\frac{\partial \mathbf{v}}{\partial \bar{\mathbf{q}}} = -\frac{1}{h}$. In contrast, the next-step position \mathbf{q} is defined only implicitly through the converged forward dynamics in Equation (6), which couples \mathbf{q} to several auxiliary variables (e.g., λ_b , λ_c , and \mathbf{p}_i). To derive partial derivatives of \mathbf{q} with respect to the previous state and other inputs, we take the total differential of Equation (6) together with the auxiliary optimality/constraint relations. This yields the coupled differential system:

$$\mathbf{A} d\mathbf{q} - \mathbf{M} d\bar{\mathbf{q}} - h \mathbf{M} d\bar{\mathbf{v}} - h^2 d\mathbf{f}_{\text{ext}} - h^2 \sum_i \mathbf{G}_i^\top \mathbf{p}_i d w_i \quad (7a)$$

$$\begin{aligned} -h^2 \sum_i w_i \mathbf{G}_i^\top d\mathbf{p}_i - h^2 \mathbf{H}_b^\top d\lambda_b - h^2 \mathbf{H}_c^\top d\lambda_c &= \mathbf{0} \\ d\lambda_b + E_b^{-1} \mathbf{H}_b d\mathbf{q} - E_b^{-1} d\mathbf{d}_b &= \mathbf{0} \end{aligned} \quad (7b)$$

$$d\lambda_c - \frac{\partial \lambda_c}{\partial \mathbf{q}} d\mathbf{q} - \frac{\partial \lambda_c}{\partial \bar{\mathbf{q}}} d\bar{\mathbf{q}} - \frac{\partial \lambda_c}{\partial \mu} d\mu = \mathbf{0} \quad (7c)$$

$$d\mathbf{p}_i - \frac{\partial \mathbf{p}_i}{\partial \mathbf{q}} d\mathbf{q} - \frac{\partial \mathbf{p}_i}{\partial w_i} d w_i - \frac{\partial \mathbf{p}_i}{\partial \xi_i} d \xi_i = \mathbf{0}. \quad (7d)$$

Equations (7c)–(7d) provide the local differential relations for frictional contact and local projections, respectively. Substituting the resulting expressions into Equation (7a) yields a linear system that relates $d\mathbf{q}$ to differentials of all inputs and parameters:

$$\begin{aligned} \mathcal{A} d\mathbf{q} &= \mathcal{K}_q d\bar{\mathbf{q}} + \mathcal{K}_v d\bar{\mathbf{v}} + \mathcal{K}_{\text{f}_{\text{ext}}} d\mathbf{f}_{\text{ext}} + \mathcal{K}_{\mathbf{d}_b} d\mathbf{d}_b \\ &\quad + \mathcal{K}_{E_b} dE_b + \mathcal{K}_\mu d\mu + \mathcal{K}_{w_i} d w_i + \mathcal{K}_{\xi_i} d \xi_i, \end{aligned} \quad (8)$$

which implicitly represents the partial derivatives of \mathbf{q} with respect to each variable on the right-hand side. The matrix blocks are

$$\mathcal{A} = \mathbf{A} - h^2 \sum_i \overbrace{w_i \mathbf{G}_i^\top \frac{\partial \mathbf{p}_i}{\partial \mathbf{q}}}^{\Delta \mathbf{A}} + \overbrace{h^2 \mathbf{H}_b^\top E_b^{-1} \mathbf{H}_b}^{\mathcal{K}_b} + \overbrace{h^2 \mathbf{H}_c^\top \left(-\frac{\partial \lambda_c}{\partial \mathbf{q}}\right)}^{\mathcal{K}_c} \quad (9a)$$

$$\mathcal{K}_q = \mathbf{M} + h^2 \mathbf{H}_c^\top \frac{\partial \lambda_c}{\partial \bar{\mathbf{q}}}, \quad \mathcal{K}_v = h \mathbf{M}, \quad \mathcal{K}_{\text{f}_{\text{ext}}} = h^2 \mathbf{I} \quad (9b)$$

$$\mathcal{K}_{\mathbf{d}_b} = h^2 \mathbf{H}_b^\top E_b^{-1}, \quad \mathcal{K}_{E_b} = -h^2 \mathbf{H}_b^\top E_b^{-1} \lambda_b, \quad \mathcal{K}_\mu = h^2 \mathbf{H}_c^\top \frac{\partial \lambda_c}{\partial \mu} \quad (9c)$$

$$\mathcal{K}_{w_i} = h^2 \mathbf{G}_i^\top (\mathbf{p}_i + w_i \frac{\partial \mathbf{p}_i}{\partial w_i}), \quad \mathcal{K}_{\xi_i} = h^2 w_i \mathbf{G}_i^\top \frac{\partial \mathbf{p}_i}{\partial \xi_i} \quad (9d)$$

In backpropagation, these partial derivatives are combined with the loss gradients $\frac{\partial L}{\partial \mathbf{q}}$ and $\frac{\partial L}{\partial \mathbf{v}}$ at the end of the time step. For example, assuming row-vector gradients, the gradient with respect to $\bar{\mathbf{q}}$ follows from the chain rule:

$$\frac{\partial L}{\partial \bar{\mathbf{q}}} = \frac{\partial L}{\partial \mathbf{q}} \frac{\partial \mathbf{q}}{\partial \bar{\mathbf{q}}} + \frac{\partial L}{\partial \mathbf{v}} \frac{\partial \mathbf{v}}{\partial \bar{\mathbf{q}}} = \underbrace{\left(\frac{\partial L}{\partial \mathbf{q}} + \frac{1}{h} \frac{\partial L}{\partial \mathbf{v}} \right)}_{\mathbf{z}^\top} \mathcal{A}^{-1} \mathcal{K}_{\bar{\mathbf{q}}} - \frac{1}{h} \frac{\partial L}{\partial \mathbf{v}}. \quad (10)$$

Rather than explicitly forming \mathcal{A}^{-1} or individual sensitivities $\frac{\partial \mathbf{q}}{\partial \bar{\mathbf{q}}}$, we introduce an adjoint variable \mathbf{z} defined by

$$\mathcal{A}^\top \mathbf{z} = \left(\frac{\partial L}{\partial \mathbf{q}} + \frac{1}{h} \frac{\partial L}{\partial \mathbf{v}} \right)^\top. \quad (11)$$

Once \mathbf{z} is computed, gradients with respect to all inputs and parameters follow from simple matrix-vector products with the corresponding right-hand-side terms in Equation (9). For all other variables $x \neq \bar{\mathbf{q}}$, since $\frac{\partial \mathbf{v}}{\partial x} = \mathbf{0}$, the gradient reduces to

$$\frac{\partial L}{\partial x} = \mathbf{z}^\top \mathcal{K}_x. \quad (12)$$

As illustrated in Figure 2, the gradients of sequential inputs (e.g., $\frac{\partial L}{\partial f_{\text{ext}}}$) are final results for the current step, the gradients of global parameters (e.g., $\frac{\partial L}{\partial E_b}$) are accumulated across time steps, and the gradients of state variables $\frac{\partial L}{\partial \mathbf{v}}$ and $\frac{\partial L}{\partial \mathbf{q}}$ are propagated to the previous step. In Sections 4.2 and 4.3, we detail the differentiation and assembly of \mathcal{K}_c , \mathcal{K}_μ , \mathcal{K}_{w_i} , \mathcal{K}_{ξ_i} and $\Delta \mathbf{A}$.

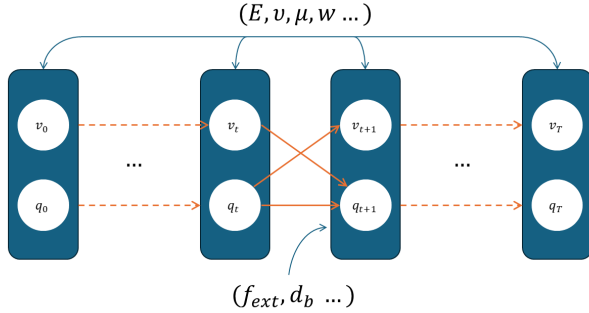


Fig. 2. Differentiation graph: gradients are obtained by implicitly differentiating the converged system in Equation (6) and solving an adjoint linear system.

4.2 NCP Contact Gradient

We first recall how δ_c depends on the current and previous states. With the tangent projector $\mathbf{P}_f := \text{Diag}(0, \mathbf{I}_{2 \times 2})$, the partial derivatives needed for Jacobian assembly are

$$\frac{\partial \delta_c}{\partial \mathbf{q}} = \mathbf{H}_c, \quad \frac{\partial \delta_c}{\partial \bar{\mathbf{q}}} = -\mathbf{P}_f \mathbf{H}_c, \quad (13)$$

which will be combined with $\frac{\partial \lambda_c}{\partial \delta_c}$ derived below to form the contact contribution to the global Jacobian blocks.

A key difficulty in differentiating Equations (6c)–(6e) is the non-smoothness induced by complementarity. In particular, the Fischer-Burmeister residual is not differentiable at $(x, y) = (0, 0)$. To obtain well-defined and numerically stable derivatives, we adopt a smoothed Fischer-Burmeister function:

$$\phi_{\text{FB}}^\epsilon(x, y) := x + y - \sqrt{x^2 + y^2 + 2\epsilon^2} \quad (14)$$

with a small $\epsilon > 0$, and use the same residual consistently in both the forward solve and the backward pass. Specifically, the zero-level set $\phi_{\text{FB}}^\epsilon(x, y) = 0$ is equivalent to the positive branch of $xy = \epsilon^2$, which is smooth for $\epsilon > 0$. In the following, we will frequently simplify derivative expressions on the zero-level set, since this is exactly the regime encountered after the converged solution:

$$\frac{\partial \phi_{\text{FB}}^\epsilon}{\partial x} = \frac{y}{x + y}, \quad \frac{\partial \phi_{\text{FB}}^\epsilon}{\partial y} = \frac{x}{x + y}. \quad (15)$$

The remaining nonlinearity in the NCP stems from the Euclidean norm $\|\cdot\|$, which intrinsically couples the two tangential components. For $\epsilon > 0$, the smoothed Fischer-Burmeister formulation ensures that the denominators involving $\|\delta_f\|$ and $\|\lambda_f\|$ are well-defined for almost all iterates after convergence. Observing from Equation (6e) that δ_f and λ_f are collinear with opposite orientations, we introduce an orthogonal transformation \mathbf{R} for each contact. This transformation rotates the contact variables into a local contact-aligned frame, thereby decoupling the normal component, the tangential magnitude, and the tangential direction. As a result, the frictional complementarity constraints admit a linearized representation with a simple, nearly block-diagonal structure. For more details on the construction of \mathbf{R} , we refer the reader to Appendix A.1. After expressing δ , λ , and their differentials in the contact-aligned basis:

$$\mathbf{R} \delta_c = \begin{bmatrix} \delta_n \\ \|\delta_f\| \\ 0 \end{bmatrix}, \quad \text{Rd} \delta_c = \begin{bmatrix} d\delta_n \\ \frac{d\|\delta_f\|}{(\delta_f \times d\delta_f)_n} \\ \|\delta_f\| \end{bmatrix} \quad (16a)$$

$$\mathbf{R} \lambda_c = \begin{bmatrix} \lambda_n \\ -\|\lambda_f\| \\ 0 \end{bmatrix}, \quad \text{Rd} \lambda_c = \begin{bmatrix} d\lambda_n \\ -\frac{d\|\lambda_f\|}{(\lambda_f \times d\lambda_f)_n} \\ \|\lambda_f\| \end{bmatrix}, \quad (16b)$$

where $(\cdot)_n$ denotes the normal component which is the only nonzero component.

Substitute Equation (15) into the differential of Equations (6c)–(6e):

$$\frac{d\delta_n}{\delta_n} + \frac{d\lambda_n}{\lambda_n} = 0 \quad (17a)$$

$$\frac{d\|\delta_f\|}{\|\delta_f\|} + \frac{d(\mu\lambda_n - \|\lambda_f\|)}{\mu\lambda_n - \|\lambda_f\|} = 0 \quad (17b)$$

$$\left(\frac{\delta_f}{\|\delta_f\|} \times \frac{d\delta_f}{\|\delta_f\|} - \frac{\lambda_f}{\|\lambda_f\|} \times \frac{d\lambda_f}{\|\lambda_f\|} \right)_n = 0. \quad (17c)$$

Comparing Equations (16) and (17) and substituting Equation (13), we obtain:

$$\frac{\partial \lambda_c}{\partial \delta_c} = -\mathbf{K}_c = -\mathbf{R}^\top \begin{bmatrix} \frac{\lambda_n}{\delta_n} & 0 & 0 \\ -\mu \frac{\lambda_n}{\delta_n} & \frac{\mu \lambda_n - \|\lambda_f\|}{\|\delta_f\|} & 0 \\ 0 & 0 & \frac{\|\lambda_f\|}{\|\delta_f\|} \end{bmatrix} \mathbf{R} \quad (18a)$$

$$\mathcal{K}_c = h^2 \mathbf{H}_c^\top \mathbf{K}_c \mathbf{H}_c, \quad \mathcal{K}_q = \mathbf{M} + h^2 \mathbf{H}_c^\top \mathbf{K}_c \mathbf{P}_f \mathbf{H}_c \quad (18b)$$

$$\frac{\partial \lambda_c}{\partial \mu} = -\mathbf{k}_\mu = -\mathbf{R}^\top \begin{bmatrix} 0 \\ \lambda_n \\ 0 \end{bmatrix}, \quad \mathcal{K}_\mu = -h^2 \mathbf{H}_c^\top \mathbf{k}_\mu. \quad (18c)$$

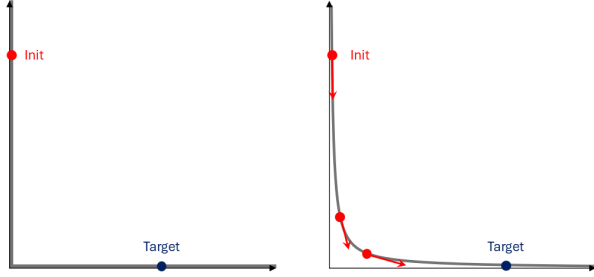


Fig. 3. The smoothed Fischer-Burmeister function transforms a hard complementarity problem (left, not differentiable at $(0, 0)$) to a smoothed one (right), providing a reliable gradient for different branch switching.

With Equation (18), we obtain a unified formulation for differentiating NCP-based contact constraints. As illustrated in Figure 3, the hard complementarity formulation admits no meaningful heuristic gradient: both finite-difference and analytical approaches collapse to zero almost everywhere. In contrast, our smoothed Fischer-Burmeister formulation provides a continuous relaxation across the non-smooth regimes of contact and separation, as well as static and kinetic friction, enabling well-defined gradients and natural transitions between regimes. We apply this smoothing consistently in both the forward and backward systems to maintain coherence between simulation and differentiation. Although the introduced smoothness theoretically perturbs the forward solution, we show through unit experiments that the resulting error remains negligible in practice (see Appendix A.2).

4.3 Local Energy Gradient

For the local projections, Equation (6f) may be differentiated into the form of Equation (19). However, this expression involves the Hessian $\nabla_{\mathbf{p}_i}^2 \zeta_i(\mathbf{p}_i, \xi_i)$, which is typically not available in closed form for many practical hyperelastic models. Instead, we differentiate the projection operator used by Projective Dynamics directly.

$$\mathbf{0} = (w_i \mathbf{I} + \nabla_{\mathbf{p}_i}^2 \zeta_i(\mathbf{p}_i, \xi_i)) d\mathbf{p}_i - w_i \mathbf{G}_i d\mathbf{q} + (\mathbf{p}_i - \mathbf{G}_i \mathbf{q}) dw_i + \frac{\partial}{\partial \xi_i} \nabla_{\mathbf{p}_i} \zeta_i(\mathbf{p}_i, \xi_i) d\xi_i, \quad (19)$$

As an illustrative example, ARAP-style projections are defined through an SVD-based mapping of the deformation gradient. Although the projection is computed algorithmically, it remains a



Fig. 4. Starting from zero applied force, we optimize a horizontal force to pull the Munchlax toward the target position (violet). The proposed heuristic gradient enables a successful transition from the sticking regime to the sliding (kinetic) friction regime.

deterministic function of the deformation as long as the SVD is non-degenerate, which enables analytic differentiation. Concretely, we assume a mild singular-value separation condition $|\sigma_i - \sigma_j| > \tau$ for $i \neq j$ with a small threshold τ . When this condition is violated (e.g., nearly repeated singular values), we propose an additional degeneracy analysis in Appendix B.4. This section derives $\frac{\partial \mathbf{p}_i}{\partial \mathbf{q}}$ for a general class of 3D hyperelastic projections under this stabilized non-degenerate setting.

In the derivation, we denote $\text{vec}(\cdot)$ as the column-stacking vectorization of a matrix, $\text{diag}(\cdot)$ as the diagonal vector of a matrix and $\text{Diag}(\cdot)$ as the diagonal matrix embedded with a vector. We also define some auxiliary matrices (exact values see Appendix B.1): $\mathbf{D}\mathbf{x} = \text{vec}(\text{Diag}(\mathbf{x}))$ and $\text{Tvec}(\mathbf{X}) = \text{vec}(\mathbf{X}^\top)$. It is straightforward to verify that $\mathbf{D}^\top \text{vec}(\mathbf{X}) = \text{diag}(\mathbf{X})$. Without loss of generality, we define the projected state vector $\mathbf{p} = \text{vec}(\mathbf{P})$, where $\mathbf{P} = \mathbf{U}\mathbf{\Theta}\mathbf{V}^\top$ is the optimized deformation gradient after local projection, which shares the same singular basis with \mathbf{F} but differs in the singular values. Denote $\boldsymbol{\sigma} = \text{diag}(\boldsymbol{\Sigma})$ and $\boldsymbol{\theta} = \text{diag}(\boldsymbol{\Theta})$. A hyperelastic model is defined by a potential function $\Psi(\boldsymbol{\theta}, \boldsymbol{\sigma})$, which is minimized by $\boldsymbol{\theta}(\boldsymbol{\sigma}) := \arg \min_{\boldsymbol{\theta}'} \Psi(\boldsymbol{\theta}', \boldsymbol{\sigma})$.

In 3-dimension deformation, \mathbf{F} and \mathbf{P} are both full-rank square matrices, while \mathbf{U} and \mathbf{V} are both orthogonal. Thus $d\mathbf{U} = \mathbf{U}\boldsymbol{\Omega}^U$ and $d\mathbf{V} = \mathbf{V}\boldsymbol{\Omega}^V$, where $\boldsymbol{\Omega}^U = -(\boldsymbol{\Omega}^U)^\top$ and $\boldsymbol{\Omega}^V = -(\boldsymbol{\Omega}^V)^\top$ are skew-symmetric. Matching the diagonal and off-diagonal elements in the differential:

$$\mathbf{U}^\top d\mathbf{F}\mathbf{V} = d\boldsymbol{\Sigma} + \boldsymbol{\Omega}^U \boldsymbol{\Sigma} - \boldsymbol{\Sigma} \boldsymbol{\Omega}^V \quad (20a)$$

$$d\Sigma_{ii} = (\mathbf{U}^\top d\mathbf{F}\mathbf{V})_{ii} \quad (20b)$$

$$\Omega_{ij}^U = \frac{\sigma_j (\mathbf{U}^\top d\mathbf{F}\mathbf{V})_{ij} + \sigma_i (\mathbf{U}^\top d\mathbf{F}\mathbf{V})_{ji}}{\sigma_j^2 - \sigma_i^2} \quad (20c)$$

$$\Omega_{ij}^V = \frac{\sigma_i (\mathbf{U}^\top d\mathbf{F}\mathbf{V})_{ij} + \sigma_j (\mathbf{U}^\top d\mathbf{F}\mathbf{V})_{ji}}{\sigma_j^2 - \sigma_i^2}, \quad (20d)$$

and

$$\mathbf{U}^\top \mathbf{dPV} = \mathbf{d}\Theta + \Omega^U \Theta - \Theta \Omega^V \quad (21a)$$

$$\begin{aligned} (\mathbf{U}^\top \mathbf{dPV})_{ij} &= \sum_k \mathbf{W}_{ik} (\mathbf{U}^\top \mathbf{dFV})_{kk} \delta_{ij} \\ &+ \frac{1}{\sigma_i^2 - \sigma_j^2} \left[(\sigma_i \theta_i - \sigma_j \theta_j) (\mathbf{U}^\top \mathbf{dFV})_{ij} \right. \\ &\left. + (\sigma_j \theta_i - \sigma_i \theta_j) (\mathbf{U}^\top \mathbf{dFV})_{ji} \right], \end{aligned} \quad (21b)$$

where δ_{ij} is the Kronecker delta, and $\mathbf{W} := \frac{\partial \theta}{\partial \sigma}$ is the derivative of singular values, which differs among hyperelastic models.

Our derivation proceeds in three steps: we differentiate the SVD-based projection $\mathbf{P}(\mathbf{F})$, express \mathbf{dP} as a linear map of \mathbf{dF} , and finally convert the result into a vectorized Jacobian $\frac{\partial \text{vec}(\mathbf{P})}{\partial \text{vec}(\mathbf{F})}$ for direct assembly into the global system. Notice that $\text{vec}(\mathbf{AXB}) = (\mathbf{B}^\top \otimes \mathbf{A}) \text{vec}(\mathbf{X})$, where \otimes is the Kronecker product. After defining

$$\mathbf{M} : \{M_{ii} = 0, M_{ij} = \frac{\sigma_i \theta_i - \sigma_j \theta_j}{\sigma_i^2 - \sigma_j^2} = \frac{1}{2} \left(\frac{\theta_i - \theta_j}{\sigma_i - \sigma_j} + \frac{\theta_i + \theta_j}{\sigma_i + \sigma_j} \right)\} \quad (22a)$$

$$\mathbf{N} : \{N_{ii} = 0, N_{ij} = \frac{\sigma_j \theta_i - \sigma_i \theta_j}{\sigma_i^2 - \sigma_j^2} = \frac{1}{2} \left(\frac{\theta_i - \theta_j}{\sigma_i - \sigma_j} - \frac{\theta_i + \theta_j}{\sigma_i + \sigma_j} \right)\}, \quad (22b)$$

we move to the column-stacking vector base and finally obtain

$$\begin{aligned} \frac{\partial \text{vec}(\mathbf{P})}{\partial \text{vec}(\mathbf{F})} &= (\mathbf{V} \otimes \mathbf{U}) [\mathbf{DWD}^\top + \text{Diag}(\text{vec}(\mathbf{M})) \\ &+ \text{Diag}(\text{vec}(\mathbf{M})) \mathbf{T}] (\mathbf{V}^\top \otimes \mathbf{U}^\top) \end{aligned} \quad (23a)$$

$$\Delta \mathbf{A} = h^2 \sum_i w_i \mathbf{G}_i^\top \frac{\partial \text{vec}(\mathbf{P})}{\partial \text{vec}(\mathbf{F})} \mathbf{G}_i \quad (23b)$$

To keep the main text concise, we defer the details of \mathbf{D} and \mathbf{T} as well as 2D formulation to Appendix B.1, the construction of \mathbf{W} for different material models B.2, and the differentiation of elastic parameters such as Young's modulus $\frac{\partial E}{\partial E}$ and Poisson's ratio $\frac{\partial \nu}{\partial \nu}$ to Appendix B.3.

The proposed formulation yields highly accurate gradients for local projection operators, which are critical nonlinear components in local-global solvers. By differentiating the projection step in a closed-form and physically consistent manner, our approach avoids common approximations, leading to stable and reliable gradient propagation even in the presence of large deformations and strong nonlinearities.

4.4 Adjoint Linear Solver

In previous sections, we derive a fully differentiable formulation for contact-involved dynamics by relaxing the non-smooth NCP constraints and expressing their differentials in a unified, contact-aligned form. This enables contact, friction, and elasticity to be consistently incorporated into the backward pass. All gradient contributions assemble into a unified sparse linear system:

$$(\mathbf{A} - \Delta \mathbf{A} + \mathcal{K}_b + \mathcal{K}_c)^\top \mathbf{z} = \left(\frac{\partial L}{\partial \mathbf{q}} + \frac{1}{h} \frac{\partial L}{\partial \mathbf{v}} \right)^\top \quad (24)$$

Although all required matrices are available, efficiently and robustly solving this adjoint system remains challenging. The matrix \mathcal{A} is large-scale and sparse, and is in general neither guaranteed to



Fig. 5. Starting from an initial guess of $E = 1 \times 10^5$ and $\nu = 0.2$ (left), we perform system identification on a curtain undergoing gravity-induced deformation. Owing to the accuracy and robustness of the proposed gradients, the optimizer is able to simultaneously recover both parameters and converges to values close to the ground truth ($E = 1 \times 10^4$, $\nu = 0.3$, right).

be symmetric positive definite nor well-conditioned. In the following, we analyze the structure of \mathcal{A} under different contact settings (contact-free, frictionless contact, and frictional contact), and introduce corresponding strategies to accelerate the adjoint solve.

4.4.1 Contact-free. We begin with the simplest setting, where no contact is involved and $\mathcal{A} = \mathbf{A} - \Delta \mathbf{A}$. As shown in Equation (19),

$$\Delta \mathbf{A} = h^2 \sum_i w_i \mathbf{G}_i^\top \underbrace{(\mathbf{I} + w_i^{-1} \nabla_{\mathbf{p}_i}^2 \zeta_i)^{-1}}_{\mathbf{J}} \mathbf{G}_i. \quad (25)$$

This expression reveals a structure analogous to $h^2 \sum_i w_i \mathbf{G}_i^\top \mathbf{G}_i$, as both arise from the aggregation of local constraints. By construction, \mathcal{A} is symmetric. Furthermore, when each ζ_i corresponds to a projection onto a manifold, its on-manifold Hessian satisfies $\nabla_{\mathbf{p}_i}^2 \zeta_i \succeq 0$, implying that all eigenvalues of $\nabla_{\mathbf{p}_i}^2 \zeta_i$ are nonnegative. As a result, $\mathbf{J}^{-1} - \mathbf{I} \succeq 0$, and $\mathbf{I} - \mathbf{J} \succeq 0$. Therefore, $\mathcal{A} = \mathbf{M} + h^2 \sum_i w_i \mathbf{G}_i^\top (\mathbf{I} - \mathbf{J}) \mathbf{G}_i \succ 0$. The resulting system is symmetric positive definite and admits a unique solution, which we solve efficiently using the conjugate gradient (CG) method.

Matrix Assembly. An observation is that the matrix pattern of $\Delta \mathbf{A}$ remains invariant since the local projective constraints are pre-defined. Moreover, the collection of elements generally remains invariant, allowing us to keep reusing the pattern of $\mathbf{A} - \Delta \mathbf{A}$ and assemble the matrix with a pre-computed mapping. Consequently, the assembly process is optimal on both memory cost and performance.

Sparse Inverse Preconditioner. To further accelerate convergence, we employ \mathbf{A}^{-1} as a preconditioner, or more concretely, its sparse inverse factorization $\mathbf{S}^\top \mathbf{S}$. This preconditioner reduces each application to two sparse matrix-vector multiplications (SpMVs), making it particularly well suited for GPU acceleration (see [35] for details).

4.4.2 Frictionless Contact. When contacts or bilateral constraints exist but without friction ($\mu = 0$), we have $\mathbf{R} \mathbf{K}_c \mathbf{R}^\top = \text{Diag}(\frac{\lambda_n}{\delta_n}, 0, 0) \succeq 0$ in Equation (18a). We denote

$$\mathcal{K} = h^2 \mathbf{H}^\top \mathbf{K} \mathbf{H} = h^2 [\mathbf{H}_b^\top, \mathbf{H}_c^\top] \text{Diag}(E_b^{-1} \mathbf{I}_b, \mathbf{K}_c) \begin{bmatrix} \mathbf{H}_b \\ \mathbf{H}_c \end{bmatrix}. \quad (26)$$

This assembled contact contribution is symmetric positive semi-definite, and therefore $\mathcal{A} = \mathbf{A} - \Delta\mathbf{A} + \mathcal{K}$ remains symmetric and, under the same assumptions as in the contact-free case, is typically positive definite.

In practice, however, \mathcal{K} can be severely ill-conditioned, which significantly degrades the effectiveness of using \mathbf{A} alone as a preconditioner. This ill-conditioning primarily arises from two sources. First, binding constraints are often enforced with very small compliance (i.e., $E_b \ll 1$) to fix or actuate points, introducing stiff directions into the system. Second, Equation (18) implies that the contact block may develop extremely large eigenvalues under large normal contact forces λ_n . Although smoothing ensures that δ_n remains strictly positive, it does not fully resolve the resulting conditioning issues. We therefore introduce several complementary strategies to address this challenge.

Jacobi Preconditioner. From Equation (18), frictionless contact contributes only to the diagonal of \mathcal{A} . In this setting, a Jacobi preconditioner based on the inverse diagonal, $(\mathcal{A}_{\text{diag}})^{-1}$, provides a simple and inexpensive means of accelerating convergence via Jacobi scaling.

Woodbury Preconditioner. Empirically, we observe that if \mathbf{A} serves as an effective preconditioner for $\mathbf{A} - \Delta\mathbf{A}$ in the contact-free regime, then augmenting it with the contact block \mathcal{K} also yields a robust preconditioner for $\mathbf{A} - \Delta\mathbf{A} + \mathcal{K}$. To apply this preconditioner efficiently, we leverage the Woodbury matrix identity:

$$\begin{aligned} (\mathbf{A} + \mathcal{K})^{-1} &= (\mathbf{A} + h^2 \mathbf{H}^\top \mathbf{K} \mathbf{H})^{-1} \\ &= \mathbf{A}^{-1} - h^2 \mathbf{A}^{-1} \mathbf{H}^\top (\mathbf{K}^{-1} + h^2 \mathbf{H} \mathbf{A}^{-1} \mathbf{H}^\top)^{-1} \mathbf{H} \mathbf{A}^{-1}, \end{aligned} \quad (27)$$

where $\mathbf{H} \mathbf{A}^{-1} \mathbf{H}^\top$ is the Delassus operator already assembled and cached during the forward simulation. The inverse \mathbf{K}^{-1} can be computed efficiently since \mathbf{K} is block-diagonal with 1×1 or 3×3 blocks. Equation (27) reduces the inverse of a large sparse system to solves with \mathbf{A}^{-1} and a dense solve in the *contact space*, whose dimension scales with the number of active contact constraints. We solve this inner system using CG.

Matrix-free Multiplication. Unlike $\Delta\mathbf{A}$, the contact contribution \mathcal{K} is dynamic. Explicitly assembling \mathcal{K} leads to an ineligible overhead. We propose using the matrix-free approach that transforms every SpMV in iterative solvers like CG as factorized multiplications:

$$\mathcal{K} \mathbf{x} = h^2 \mathbf{H}^\top \mathbf{K} \mathbf{H} \mathbf{x} = h^2 \mathbf{H}^\top (\mathbf{K} (\mathbf{H} \mathbf{x})) \quad (28)$$

without explicitly assembling the matrix. Consequently, the full SpMV for \mathbf{A} turns to a hybrid way that includes $\mathbf{A} - \Delta\mathbf{A}$ with assembled matrix and \mathcal{K} with matrix-free operations.

4.4.3 Frictional Contact. When friction is present ($\mu > 0$), the assembled contact contribution in Equation (18) is generally non-symmetric, and the resulting adjoint system is no longer guaranteed to be SPD. Accordingly, we switch from CG to Generalized minimal residual method (GMRES), while retaining the same block-structured assembly and preconditioning strategy.

Summary. Overall, the proposed adjoint solvers and preconditioning strategies are designed to be highly amenable to parallel execution. All major components—including matrix assembly, sparse

matrix–vector multiplications, matrix-free contact operators, and block-diagonal inverses—exhibit strong data parallelism and minimal synchronization. In particular, the reuse of invariant sparsity patterns, the reliance on local block operations, and the reduction of global solves to contact-space systems enable efficient GPU implementations. As a result, our approach scales well to large contact-rich simulations while maintaining robust convergence across different contact regimes. In Section 5.2, we evaluate the proposed solvers and preconditioners with a detailed analysis of convergence behavior and computational performance.

5 Results

This section evaluates and discusses quantitative results for the proposed differentiable simulation method for deformable materials (Section 4). All simulations are conducted on a workstation equipped with an Intel® Ultra 9 285K CPU and an NVIDIA GeForce RTX 5090 GPU with 32 GB RAM. We first validate the correctness of our analytical gradients by comparing them against finite-difference ground-truth gradients across a range of environments and tasks, including system identification and optimal control. Next, we evaluate the convergence behavior and runtime performance of our linear solver under diverse settings, with several alternative linear solvers serving as baselines. Finally, we demonstrate a complex, practical cable-driven manipulation task to present the high fidelity, where the control sequence for a deformable robot is optimized using gradients provided by our differentiable simulator.

5.1 Gradient Analysis

Although differentiable simulation provides gradients, it remains an open question whether these gradients align with real-world physics and can reliably support practical downstream tasks. We argue that the answer hinges on the fidelity of the forward simulator, which serves as the bridge between physical reality and differentiation. Our analytical gradients are derived by directly differentiating the fully solved forward dynamics, without additional approximations or heuristic modifications. Therefore, when the forward simulation accurately matches real-world physical laws after convergence, the resulting gradients inherit this accuracy and reduce the sim-to-real gap. As a reference, we compute the finite-difference gradient of the forward simulation,

$$\left(\frac{\partial L}{\partial x}\right)_{\text{FD}} := \frac{L(x + \eta) - L(x - \eta)}{2\eta}, \quad (29)$$

using a small step size $\eta \ll 1$. We regard this as the ground-truth gradient and evaluate the consistency of our analytical gradient against it.

To obtain a comprehensive assessment, we design a suite of unit tests, each targeting a specific component of the differentiation pipeline—from elasticity to frictional contact—by solving a corresponding optimization problem using only basic gradient descent. We intentionally avoid advanced optimizers (e.g., quasi-Newton methods) so that convergence depends primarily on the quality of the gradients. Unless stated otherwise, each experiment optimizes a single scalar parameter from an initial value toward a prescribed target. We use a final state matching objective,

$$L = \|\mathbf{q}_{\text{final}} - \mathbf{q}_{\text{target}}\|^2, \quad (30)$$

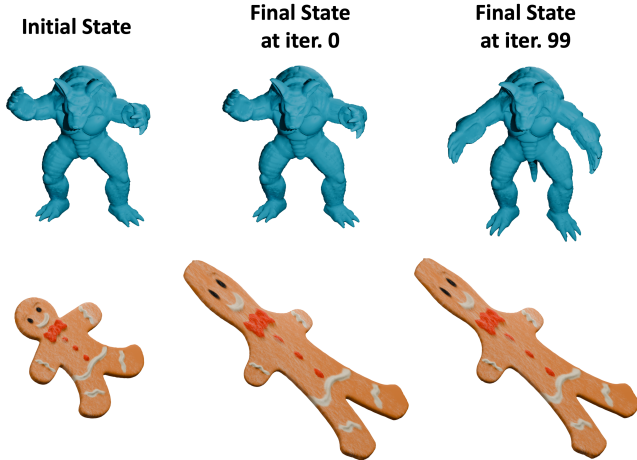


Fig. 6. Gradient-based of stiffness (top) and Poisson’s ratio (down) in contact-free settings. We recover volumetric stiffness and Poisson’s ratio across linear and nonlinear elastic models, demonstrating that the proposed gradients capture long-range elastic coupling and nonlinear parameter sensitivities.

defined as the sum of squared distances between the final positions of all points under the current parameter value and those under the target value at the end of the time horizon.

5.1.1 Elasticity. We first isolate elasticity by disabling all contact interactions, so that the dynamics are governed solely by internal elastic forces. In this contact-free setting, we perform multiple system identification runs to verify that the gradients capture the long-range coupling introduced by elasticity.

As shown in Figure 6, with a high initial stiffness $k_s = 2E+5$, the arms are merely static and keep raising. We manage to optimize it toward a pretty low target $\hat{k}_s = 1E+4$, so that the Armadillo are bringing its arm down to the front, like “waving goodbye”. Similarly, we then fix the stiffness at $k_s = 2E+4$ and examine its motion under variant force field, i.e., drifting in a wind. After optimizing the uniform wind force f_{wind} from zero, the Armadillo finally stabilizes to a “flying” pose under target strong wind $\hat{f}_{\text{wind}} = 50$ (Figure 7).

To further extend the elasticity tests beyond volumetric stiffness, we next move to cloth deformation and study gradients for bending coefficient. Unlike stiffness—which defines per-element constraints and energy in each tetrahedron or triangle—cloth bending introduces longer-range coupling across the surface and tends to be more susceptible to gradient inaccuracies. We again perform system identification on the bending coefficient k_b of a rectangular cloth patch by pulling its two ends together, causing the patch to fold into an U-shaped bend (Figure 7). At the beginning, the cloth is overly stiff ($k_b = 5E+2$): instead of sagging, it tends to bow outward toward the two sides, leaving the mid-span relatively lifted and failing to form a deep U-shape. As optimization softens the cloth, the strip progressively drops under its own weight and the profile straightens into a deeper, well-filled U-shaped arc, converging to the target $\hat{k}_b = 1E+1$.

We next move beyond the ARAP-based models and evaluate gradients under a nonlinear hyperelastic constitutive law. This transition is important because ARAP can be viewed as a rotation-invariant, quadratic-style energy that is widely used for robust shape preservation, but it does not fully represent physically grounded stress–strain relations. In contrast, a Neo-Hookean model is derived from continuum mechanics and introduces genuinely nonlinear coupling through the deformation gradient, especially under large strain. As a result, both the forward dynamics and the corresponding gradients become more challenging: stresses depend nonlinearly on the state, parameter sensitivities are no longer simple scalings, and the optimizer must rely on accurate derivatives to navigate a more curved objective landscape.

In this nonlinear regime, Poisson coupling offers an especially sensitive way to stress-test gradient quality. Unlike stiffness-like parameters that often mainly scale the overall deformation magnitude, Poisson’s ratio ν governs the transverse response and couples orthogonal directions, so even small gradient errors can manifest as visibly incorrect lateral contraction or expansion. To probe this effect, we adopt a Gingerbread-Man thin shell under a Neo-Hookean model and identify ν from 0.1 to $\tilde{\nu} = 0.4$ by matching the final positions. Concretely, we grasp the model at its head and feet, and pull it laterally outward, producing strong in-plane stretching with pronounced transverse deformation (Figure 6); the resulting waist width provides a clear cue, with a thinner waist indicating a higher Poisson’s ratio due to stronger volume preservation.

Figures 10a–10d show that, across the above elasticity-only experiments, our analytical gradients match the ground-truth derivatives essentially perfectly—consistently for both soft and stiff materials, under mild and large deformations, and from simple to more advanced elastic models. Throughout the optimization, both the loss (plotted on a logarithmic scale) and the identified parameters converge smoothly and steadily, without unexpected fluctuations. These results indicate that the gradients remain accurate and informative across a wide range of elastic regimes.

Finally, we move to a two-parameter identification problem under nonlinear hyperelasticity. We simulate a Neo-Hookean curtain with its upper edge fixed, allowing the rest to drape under gravity (Figure 5). The resulting deformation shows both vertical stretch and lateral narrowing: Young’s modulus E mainly sets the overall compliance along gravity, while Poisson’s ratio ν governs transverse contraction. Crucially, these effects are coupled—through the nonlinear constitutive response, E and ν interact and jointly determine the full deformation.

Compared with the single-parameter unit tests, this joint identification setting is more demanding. The objective depends on coupled parameter directions, and discrepancies accumulated over time can be explained by different combinations of (E, ν) , making the landscape harder to optimize. Figure 9 shows that our optimizer still converges smoothly in both parameters, reaching $(\hat{E}, \hat{\nu}) = (1E+4, 0.3)$ from $(1E+5, 0.2)$ under the same evaluation protocol.

Taken together, these elasticity-only experiments validate our analytical gradients under both single- and multi-parameter identification, and under both simple and nonlinear constitutive laws.

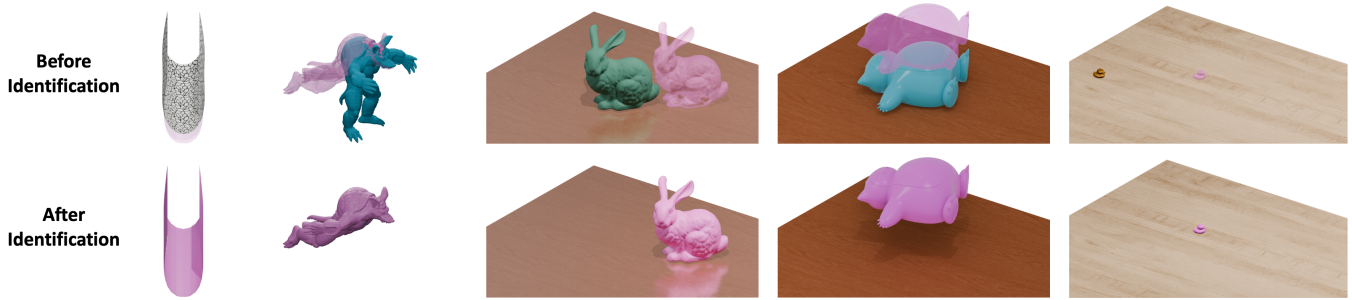


Fig. 7. Experimental validation before (**top row**) and after (**bottom row**) identification across five different physical scenarios. The top row shows the simulation using initial guesses, while the bottom row utilizes the identified parameters, achieving perfect alignment with the target (pink). The columns from left to right correspond to the identification of: (1) bending constraint, (2) wind force, (3) friction factor, (4) lifting force, and (5) initial velocity with friction.

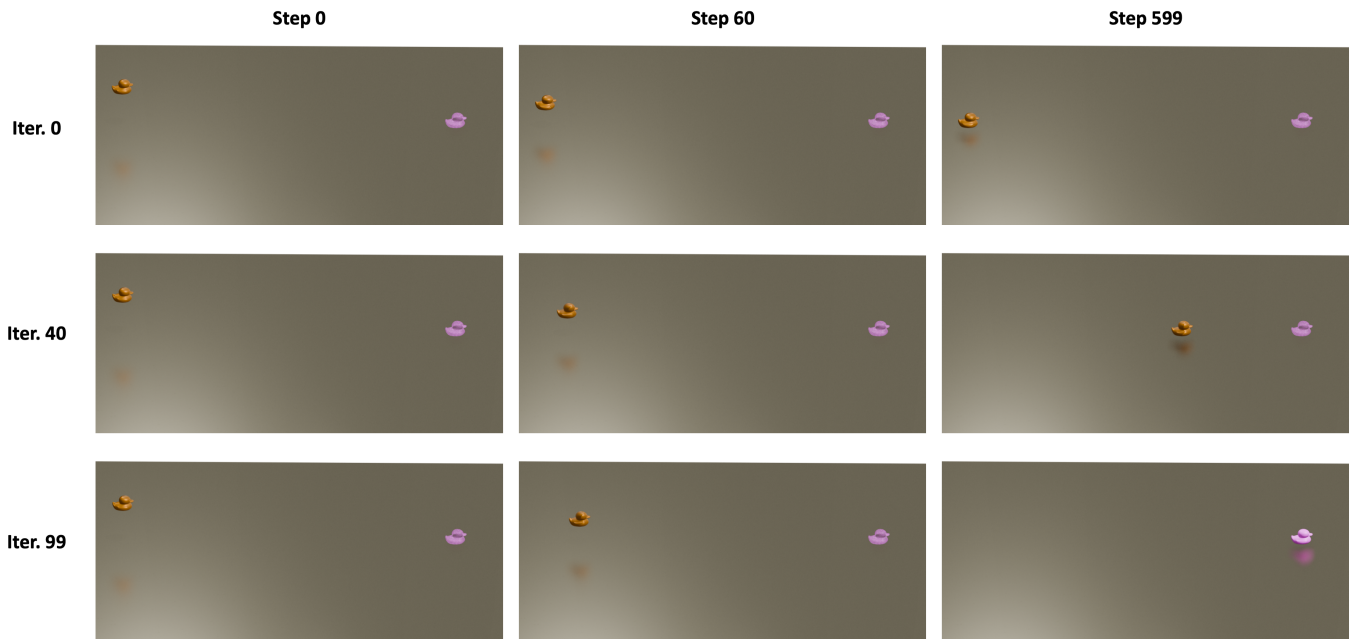


Fig. 8. We launch an elastic rubberduck horizontally onto a frictionless surface, involving frictionless contact dynamics. The optimization objective is the configuration indicated by the pink silhouette. Given the global state and target vertex positions, our method successfully optimizes the trajectory to reach the target at step 599 in 100 iterations.

With this baseline established, we next turn to contact and friction, where regime switching introduces additional challenges for gradient accuracy.

5.1.2 Contact. Compared with elasticity, differentiating frictional contact is fundamentally more difficult because the forward dynamics are inherently mode-dependent. In the normal direction, interaction switches between separation and contact; in the tangential direction, friction switches between sticking (static friction) and sliding (kinetic friction). As a result, the mapping from parameters/controls to states is only piecewise smooth: it takes different forms across branches, and many optimization-critical signals appear right at the branch boundaries.

A common approach is to make these branches explicit (e.g., via active sets) and differentiate case-by-case. However, this can easily derail gradient-based optimization. First, it often blocks gradient flow: when a branch is imposed as a hard constraint (for instance, sticking encoded as zero relative tangential motion), the associated variations are effectively excluded from the differential system, so the gradient signal can become weak or even vanish along important directions. Second, explicit branching makes it hard to move between branches: once the iterate is linearized inside one branch, local gradients usually provide little guidance for crossing into another (e.g., from sticking to sliding), which leads to mode-locking and poor long-horizon behavior.

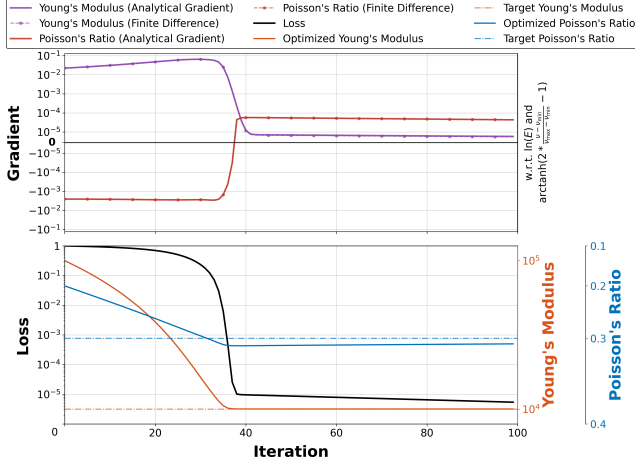


Fig. 9. **Two-parameter system identification under Neo-Hookean hyperelasticity.** We jointly optimize Young’s modulus E and Poisson’s ratio ν for the hanging-curtain setup. **Top:** analytical gradients closely match finite-difference references throughout the run, including the coupled transition around the rapid descent phase. **Bottom:** the loss (logarithmic scale) decreases smoothly as (E, ν) converge to their targets, illustrating stable multi-parameter optimization despite nonlinear parameter coupling.

In our method, we avoid explicit branch enumeration by writing normal contact and Coulomb friction in a single residual system, and then differentiating the converged forward solve via implicit differentiation. Using a smooth NCP formulation (based on a smoothed Fischer–Burmeister function) in both the forward and backward passes yields well-defined and numerically stable derivatives near contact transitions. The experiments below are designed to stress exactly this point, checking whether the gradients remain informative in contact-rich trajectories where branch changes are unavoidable.

We first examine whether gradient-based optimization can cross the contact–separation boundary by placing a heavy Snorlax on a smooth table and attempting to lift it to a target height using an upward force $\tilde{F}_{\text{lift}} = 20$ (Figure 7). When $F_{\text{lift}} < G$ (G is the gravity), the Snorlax stays in contact, as the table’s normal force balances the residual load $G - F_{\text{lift}}$. In our experiment, we initialize from $F_{\text{lift}} = 0$, i.e., deep in the contact regime.

A trivial branch-wise treatment would keep the system on the contact branch at initialization. Because the Snorlax is heavy, small perturbations of F_{lift} around zero are fully absorbed by the support force, leaving the forward trajectory unchanged; consequently, the objective is locally flat and the gradient with respect to F_{lift} becomes (nearly) zero, making it impossible for gradient descent to cross the boundary. In contrast, our method (Figure 10f) yields a small but consistently nonzero gradient that keeps pushing F_{lift} upward. This is clearly reflected in the optimization traces: while the loss remains almost constant for a long period, the optimized force increases steadily until it reaches G , at which point the dynamics switch to the separation regime.

After separation, the sensitivity of the height objective to F_{lift} becomes much stronger, and the gradient magnitude increases sharply. Since we use a relatively large learning rate to escape contact, the

optimization may exhibit brief oscillations immediately after the switch, but F_{lift} quickly settles to the target $\tilde{F}_{\text{lift}} = 10$. Notably, throughout the entire run—on either branch, during both the flat phase and the transient oscillations—our analytical gradients closely match finite differences. This agreement indicates that the gradients arise directly from our derivation of the forward dynamics, rather than from any extra heuristics designed to “guide” the optimizer across the boundary.

We next validate branch switching between static and kinetic friction. Similar to the lifting test, we apply a horizontal pulling force to drag an object—initially at rest—across a rough table toward a target position. We consider two identification tasks: optimizing the force magnitude for previously mentioned Munchlax (Figure 4), and optimizing the friction factor for a Stanford bunny (Figure 7). In both cases, the initialization lies in the static-friction regime, where a branch-wise formulation would predict zero gradients because small parameter changes do not alter the sticking trajectory.

As in the contact–separation experiment, the loss first stays on a plateau until the system transitions into kinetic friction. The optimized variable then exhibits a clear staged convergence: it changes slowly while the object remains stuck, shifts rapidly once sliding begins, and finally settles near the target value after entering the kinetic regime.

A key difference from the frictionless setting is that friction amplifies forward-simulation errors, making finite-difference gradients much less reliable (Figure 10e and 10g). When the finite-difference step η is too small, the induced trajectory change can be masked by simulation noise and solver tolerances, leading to highly fluctuating and distorted gradient estimates. In contrast, our analytical gradients remain stable and informative through both regimes and across the switching point, enabling the optimizer to make consistent progress even when finite differences become numerically fragile.

Finally, we move beyond single-switch tests and consider a longer, contact-rich motion with frequent branch changes. We use an elastic (ARAP) rubber-duck model, released horizontally in mid-air, and optimize its initial velocity to match a target termination position (Figure 7). The target motion is deliberately multi-stage: the duck first travels forward in free flight, then drops under gravity, impacts the ground with a small rebound, and finally enters frictional sliding until it comes to rest.

This setup induces repeated switching in both the normal and tangential contact modes. Around the first impact, contact points appear and disappear rapidly; at the same time, the resulting impulses and frictional forces interact through the duck’s elasticity, since forces at different contact locations are coupled by the shared deformable body. The combination yields a highly non-smooth and strongly coupled optimization landscape, providing a stringent stress test for gradient fidelity over long horizons. As a comparison, we also include a frictionless variant with the same setup and the same target initial velocity.

Experiments show that, no matter with or without friction, the optimized initial velocity converges reliably to the target value. In the frictionless case, where the final position is proportional to the initial velocity, the finite-difference estimates are effectively exact

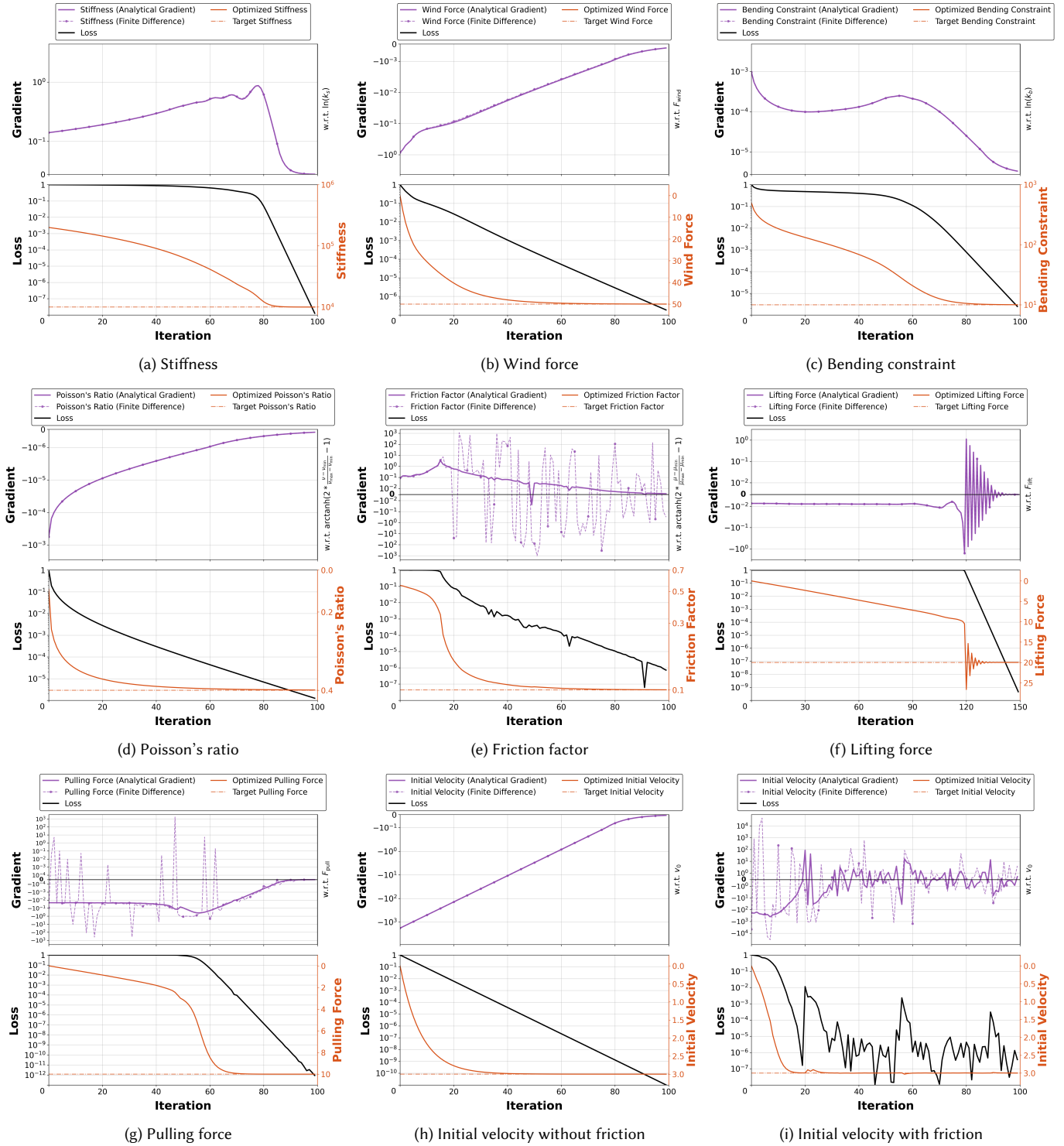


Fig. 10. **Gradient unit tests for elasticity and contact.** Each panel reports a gradient-based identification task: (a) stiffness, (b) wind force, (c) bending coefficient, (d) Poisson's ratio, (e) friction factor, (f) lifting force, (g) pulling force, and initial-velocity identification (h) without friction and (i) with friction. In each panel, the **top** subplot compares analytical gradients with finite-difference references (with “w.r.t.” indicating the reparameterized optimization variable), and the **bottom** subplot shows the loss and the corresponding parameter trajectory over iterations.

and insensitive to the step size (Figure 10h). As reported in Table 1, the finite differences and analytical gradients agree to numerical precision (zero MRE). Consistent with this linear setting, the loss decreases exponentially, appearing as an approximately straight line on the logarithmic plot, which matches the observed curves.

With friction, the dynamics become markedly more challenging due to repeated stick–slip transitions and amplified numerical error, making finite-difference estimates unreliable and the loss curve visibly less smooth (Figure 10i). Nevertheless, our analytical gradients remain stable and informative, consistently providing a useful descent direction and driving the optimization to converge even in this contact-rich, frictional setting.

5.1.3 Quantitative Statistics. In this section, we provide quantitative statistics that summarize the experiments above. To compare convergence behavior across different phases of optimization and to quantify the relative discrepancy between analytical and finite-difference gradients, we report the following metrics. Let $L^{(i)}$ denote the loss value at iteration $i \in \{0, \dots, T\}$. We first report $t_{0.5}$ and $t_{0.9}$, defined as the iteration percentages at which the optimization achieves 50% and 90% of the total loss decrease:

$$t_p := \frac{1}{T} \min \{i : L^{(0)} - L^{(i)} \geq p(L^{(0)} - L^{(T)})\}, \quad p \in \{0.5, 0.9\}. \quad (31)$$

We then define the early/mid/late (E/M/L) stages as iteration index ranges separated by $t_{0.5}/t_{0.9}$. To characterize stage-wise progress, we report the normalized area-under-curve of the loss within each stage,

$$\text{AUC}|S := \frac{1}{|S|} \sum_{i \in S} \frac{L^{(i)} - L^{(T)}}{L^{(0)} - L^{(T)}}, \quad S \in \{E, M, L\}, \quad (32)$$

where lower values indicate faster convergence within the corresponding phase. At last, we quantify gradient agreement by the mean relative error (MRE) between analytical gradients $g_{\text{ana}}^{(i)}$ and finite-difference gradients $g_{\text{fd}}^{(i)}$ within each stage:

$$\text{MRE}|S := \frac{1}{|S|} \sum_{i \in S} \frac{\|g_{\text{ana}}^{(i)} - g_{\text{fd}}^{(i)}\|}{\|g_{\text{fd}}^{(i)}\| + \epsilon_g}, \quad S \in \{E, M, L\}, \quad (33)$$

with a small ϵ_g to avoid division by zero. We summarize these statistics together with the key task specifications (shape, constitutive model, friction setting, and optimized parameter) in Table 1.

It enables a more quantitative reading of gradient quality and its impact on optimization dynamics. First, the stage-wise loss AUC provides a compact indicator of early “plateaus”: a larger AUC|E means that the loss stays high for longer in the early stage. Two mechanisms dominate these plateaus in our suite. In the stiffness test, the plateau mainly comes from starting in an overly stiff regime: the optimization must first soften the material substantially before the deformation becomes responsive enough to reduce the loss. In the lifting and pulling tasks, the plateau is instead caused by mode dependence: the optimizer must push the system across a branch boundary (contact–separation or static–kinetic friction), before which the forward state (and thus the loss) changes only weakly. These behaviors are also reflected by the gap $t_{0.9} - t_{0.5}$: once a mode switch is triggered, the remaining error typically collapses

quickly, yielding a smaller gap than cases where the loss remains gradually informative throughout.

The gradient-error statistics further align with the qualitative behavior observed in the plots. Notably, the cases with the largest MRE (often on the order of 10^0) are precisely those involving friction. As shown in the corresponding curves, finite-difference gradients become highly unstable in these settings, so a large MRE primarily reflects the unreliability of the finite-difference reference rather than a failure of our analytical gradients. In all remaining cases, MRE remains very small and the finite-difference curves are smooth and consistent, indicating that our analytical gradients closely match a high-quality numerical reference and reliably drive convergence.

5.2 Solver Performance

The unit tests above demonstrate that our analytical gradients closely match finite-difference ground truth. However, this agreement relies on a fundamental prerequisite: both the forward and backward solves must converge. We do not further analyze the convergence and performance of the forward simulation, as it is beyond the scope of this paper. Instead, we focus on the adjoint linear system in the backward pass (Equation (11)), whose solution quality directly impacts gradient accuracy and practical usability.

The backward solve influences our results in two critical ways. First, if the required number of iterations is large or varies significantly across scenarios, a fixed and limited iteration budget may be insufficient in harder cases, leading to non-convergence and inaccurate gradients. Second, even when convergence is eventually achieved, slow solves can render differentiable simulation prohibitively expensive for downstream optimization. The solver designs and preconditioning strategies proposed in Section 4.4 are intended to address both issues by providing controlled and consistently fast convergence across a wide range of regimes.

We evaluate this goal under three representative regimes of increasing difficulty: contact-free, frictionless contact, and frictional contact, corresponding respectively to SPD, ill-conditioned SPD, and ill-conditioned asymmetric systems. To avoid redundant setups, we reuse the unit-test scenarios from the previous subsection as solver benchmarks: Armadillo stiffness identification for the contact-free regime, the Snorlax lifting task for frictionless contact, and the Munchlax pulling-and-sliding task for frictional contact. This choice keeps the physical setup fixed while isolating the behavior of the backward linear solver.

Within each regime, we benchmark Krylov solvers (CG for SPD systems and GMRES for nonsymmetric systems) combined with different preconditioners, including the Sparse-Inverse Preconditioner, Jacobi Preconditioner, and Woodbury Preconditioner proposed in Section 4.4. We also report the performance of the backward solver used in DiffPD [6] and DiffCloth [15] as a reference. Notably, this solver is not a Krylov method; instead, it employs a semi-implicit fixed-point iteration of the form $\mathbf{x}^{k+1} = \mathbf{A}^{-1}(\mathbf{b} - (\mathcal{A} - \mathbf{A})\mathbf{x}^k)$.

Results and Analysis. Figure 11 summarizes convergence behavior across all regimes. In the contact-free case, the Sparse-Inverse Preconditioned CG achieves the fastest convergence in both iteration count and runtime, significantly outperforming unpreconditioned CG and the semi-implicit baseline. While the semi-implicit solver

Table 1. **Statistics of gradient accuracy and optimization behavior across elasticity and contact tasks.** We evaluate a suite of identification problems spanning elasticity (left) and contact (right), and report both stage-wise optimization behavior and gradient agreement. Stage-wise behavior is characterized by $t_{0.5}$ and $t_{0.9}$, the iteration percentages required to achieve 50% and 90% of the total loss decrease, and by the normalized loss area-under-curve over early/mid/late iterations (AUC|E, AUC|M, AUC|L). Gradient agreement is summarized by the mean relative error between analytical and finite-difference gradients within each stage (MRE|E, MRE|M, MRE|L; lower is better). For completeness, the table also lists the key task specifications for each column (e.g., shape and constitutive model), with checkmarks/crosses indicating the presence/absence of friction and learning rate is defined after reparameterization (Figure 10).

Target	Elasticity					Contact				
Shape	Armadillo		Cloth	GB-Man	Curtain	Bunny	Snorlax	Munchlax	YR-Duck	
Model	ARAP		ARAP + B.	NH	NH + B.	ARAP	ARAP	ARAP	ARAP	
Vertex	1.2k		1.0k	2.0k	0.5k	1.5k	1.0k	1.0k	0.9k	
Friction	—		—	—	—	✓	✗	✓	✗	✓
Opt. Variable	k_s	F_{wind}	k_b	ν	(E, ν)	μ	F_{lift}	F_{pull}	v_0	
Learn. Rate	0.1	8	300	600	(1.5, 3)	0.05	10	2	2E-4	1E-3
Init. Value	2E+5	0	5E+2	0.1	(1E+5, 0.2)	0.55	0	0	0	0
Target Value	1E+4	50	1E+1	0.4	(1E+4, 0.3)	0.1	20	10	3	3
$t_{0.5}$	68%	3%	17%	2%	27%	17%	80%	55%	4%	8%
$t_{0.9}$	80%	11%	62%	4%	34%	20%	82%	59%	11%	11%
AUC E	58.33	2.12	9.98	1.19	21.99	15.90	79.91	53.80	2.84	6.03
AUC M	3.62	1.43	16.41	0.18	1.65	0.45	0.25	0.78	1.33	0.57
AUC L	0.09	0.69	0.42	0.27	0.04	0.35	0.03	0.10	0.27	0.08
MRE E ↓	5.74E-3	1.26E-3	1.42E-5	9.21E-3	4.76E-7	1.26E-1	2.14E-3	8.15E-1	0	8.65E-1
MRE M ↓	1.75E-2	1.8E-2	3.73E-4	7.97E-3	4.98E-7	3.16E-1	0	4.39E-1	0	3.22E-0
MRE L ↓	3.01E-3	5.38E-2	1.01E-3	6.97E-3	8.57E-3	9.69E-1	0	1.30E-0	0	5.95E-0

benefits from the guidance of \mathbf{A}^{-1} and converges reasonably well, it remains slower than Sparse-Inverse Preconditioned CG, which additionally exploits rapid residual reduction in the Krylov subspace.

In the frictionless contact regime, where the system is deliberately ill-conditioned due to large contact contributions, several notable behaviors emerge. The semi-implicit solver becomes unreliable and diverges within a few iterations. Using \mathbf{A}^{-1} alone as a preconditioner leads to oscillatory convergence, likely because the contact term \mathcal{K} dominates the system and undermines the effectiveness of \mathbf{A}^{-1} as a global guide. In contrast, the Woodbury Preconditioned CG exhibits strong robustness and converges to high accuracy within a small number of iterations. However, due to its higher per-iteration cost, Jacobi Preconditioned CG achieves better overall runtime performance on the GPU, benefiting from its extremely low overhead and effective diagonal scaling for diagonally dominant but ill-conditioned systems.

In the frictional contact regime, where the system becomes asymmetric, we replace CG with GMRES. The observed trends closely mirror those of the frictionless case. The semi-implicit solver again diverges rapidly, while preconditioning solely with \mathbf{A}^{-1} leads to unstable and oscillatory convergence. Woodbury Preconditioned GMRES remains the most robust in terms of convergence, whereas Jacobi Preconditioned GMRES offers the best runtime performance when per-iteration cost is taken into account.

Summary. Overall, these experiments confirm that robust adjoint solves in contact-involved settings require both appropriate Krylov solvers and carefully designed preconditioners. Sparse-Inverse and Woodbury preconditioners provide strong convergence guarantees

across regimes, while Jacobi preconditioning offers an attractive performance–robustness trade-off, particularly on GPUs. In contrast, semi-implicit solvers and naive preconditioning strategies exhibit limited effectiveness for the adjoint systems arising from our formulation in Equations (18) and (11).

5.3 Application in Robot Control

In this subsection, we demonstrate the practical value of our differentiable simulator on challenging soft-robot control tasks. Even with a minimal, first-order optimizer, our method can solve complex long-horizon objectives quickly and reliably, highlighting that the key enabler is accurate and stable gradients rather than sophisticated optimization heuristics.

Both experiments center on a tendon-driven, tentacle-like soft manipulator. As illustrated in Fig. 12, the robot is discretized into a chain of compliant segments, connected by internal elastic elements, and actuated through multiple cables routed along its body. We designed a complex symbol-driven optimization experiment to verify the operational feasibility of this arm in differentiable simulation (Fig. 12).

Cable actuation is indirect: the control input is a change in cable length, which generates distributed internal forces, bends the backbone, and produces highly nonlinear deformations. Unlike articulated rigid robot arms (e.g., Franka), where inverse kinematics and motion planning often admit simple geometric formulations, soft manipulators exhibit strong coupling between actuation and deformation. A small change in one cable can affect the entire shape, interact with other cables through elasticity, and produce contact

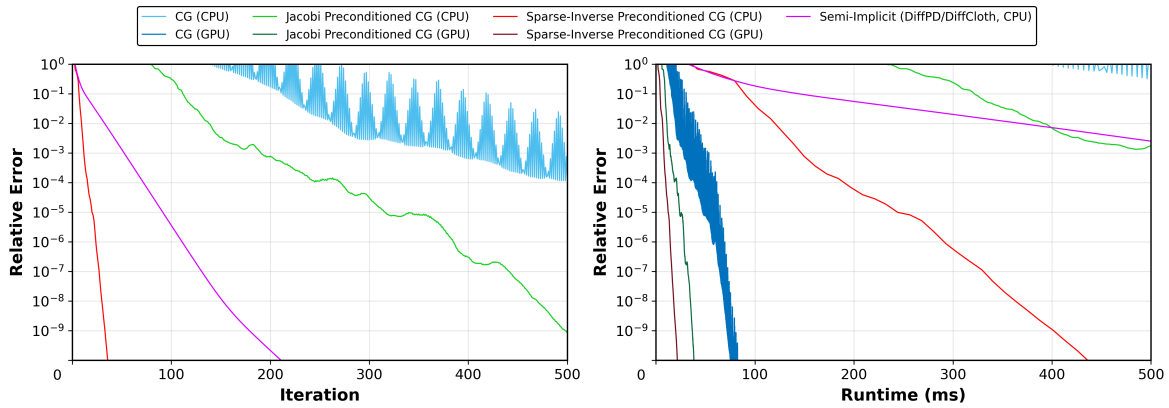
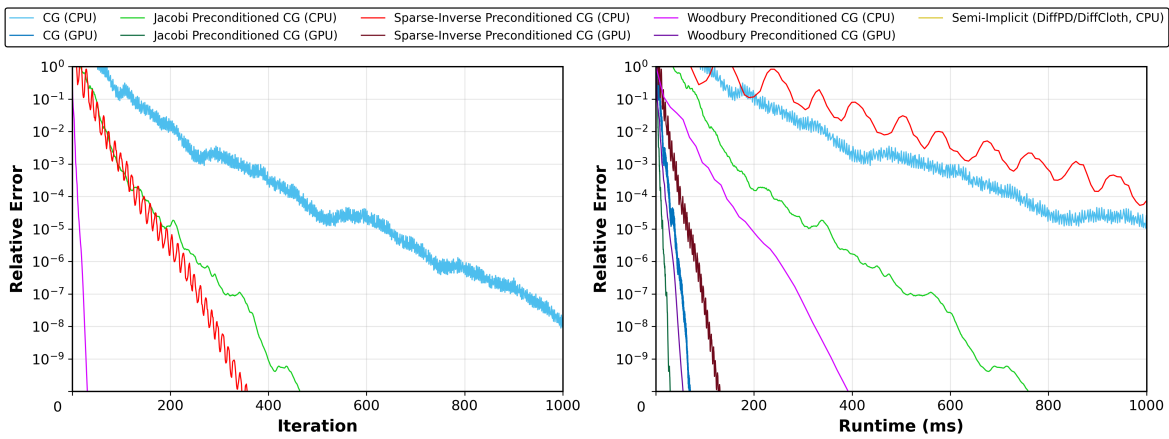
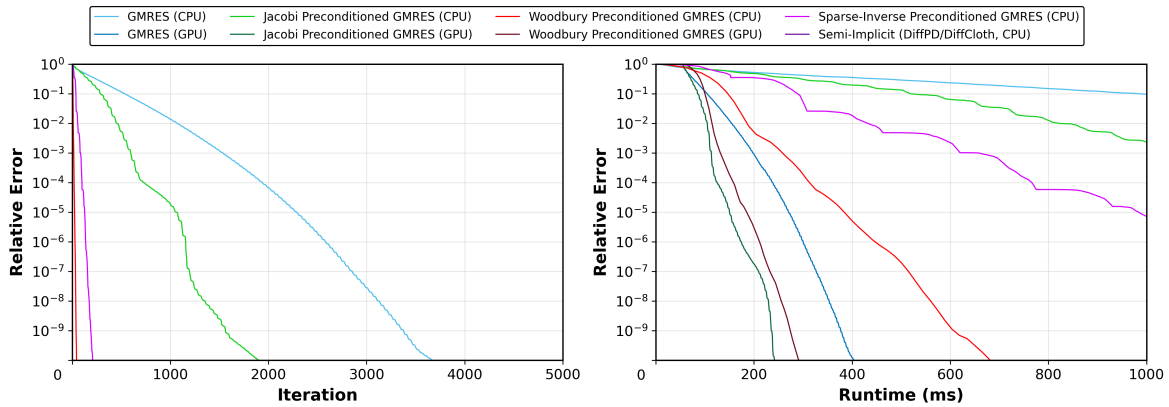
(a) Convergence comparison in contact-free regime, $\text{norm}(\mathbf{A} - \Delta\mathbf{A}) = 7.79426e + 08$.(b) Convergence comparison in frictionless contact regime, $\text{norm}(\mathbf{A} - \Delta\mathbf{A}) = 36539.1$, $\text{norm}(\mathcal{K}) = 111163$. The Semi-Implicit diverges in first iterations.(c) Convergence comparison in frictional contact regime, $\text{norm}(\mathbf{A} - \Delta\mathbf{A}) = 366299$, $\text{norm}(\mathcal{K}) = 23729.3$. The Semi-Implicit diverges in first iterations.

Fig. 11. Convergence comparison of different adjoint solvers and preconditioners. We report relative residual error versus iteration count (left) and wall-clock runtime (right) under (a) contact-free, (b) frictionless contact, and (c) frictional contact regimes. Different curves correspond to different solver and preconditioning strategies executed on CPU or GPU (see legend).

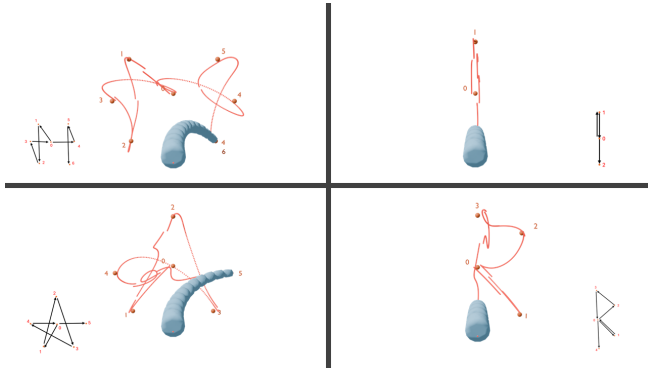


Fig. 12. Optimization-based tracking using a 4-cable elastic trunk. We discretize "SIGGRAPH" characters into keypoints and optimize cable tensions using differentiable simulation. The GPU-accelerated pipeline completes the complex tracking task within 1 hour. We shows "H", "A", "I" and "R" here.

events with the environment. Moreover, the state space is high-dimensional and the input-output relation is difficult to characterize analytically: it is generally unclear how a particular cable command will move the end-effector, how much it will move, and what secondary deformations will be induced along the body.

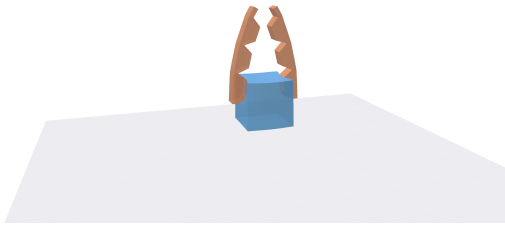


Fig. 13. Gradient-based control of a cable-driven soft gripper for object grasping. The optimized cable actuation exploits fully coupled elastic deformation and contact to achieve stable grasps.

Our differentiable simulator directly fills this gap by providing gradients of task objectives with respect to cable controls through the fully coupled dynamics, including elasticity and contact. This enables straightforward gradient-based optimization of control sequences without requiring an explicit response model, handcrafted Jacobians, or simplified kinematic assumptions. We evaluate this capability in two representative tasks: (i) a soft robotic gripper that grasps and manipulates objects (Figure 13), and (ii) treating a toy elephant trunk as a soft arm and optimizing its cable controls to write on a wall. We describe the task setups and results in the following paragraphs.

6 Limitations and Future Work

For limitations, firstly, the validity of our gradients relies on the smoothing parameter ϵ within the NCP formulation. While we observe that small ϵ values induce negligible physical error, extremely

stiff contact constraints may still require careful parameter tuning to balance numerical conditioning with physical accuracy. Second, although our linear solvers are optimized for GPUs, the global coupling inherent in implicit integration means computational cost scales super-linearly with degrees of freedom. For extremely high-resolution meshes, the memory footprint of sparse factorizations remains a potential bottleneck. Our current formulation also assumes a fixed topology; differentiating through topological changes, such as fracture or tearing, involves discontinuous state-space jumps that our continuous relaxation does not currently address.

Looking forward, several research avenues emerge from the current framework. In the context of sim-to-real transfer, the high fidelity of the proposed frictional contact model suggests it could be instrumental in narrowing the reality gap. Its application within hardware-in-the-loop pipelines appears particularly promising for robotics tasks requiring precise manipulation and interaction with complex environments. Beyond simulation accuracy, the framework's differentiability and performance indicate strong potential for Model Predictive Control (MPC). The ability to provide analytical gradients through contact events renders the solver a viable candidate for integration into real-time, nonlinear control strategies for soft robotics. From a systems perspective, adapting the unified adjoint formulation to distributed multi-GPU architectures represents a significant opportunity for scalable computing. Future exploration into compatible domain decomposition techniques would be essential for extending these capabilities to large-scale, high-resolution physical simulations.

Acknowledgments

This work was supported in part by the NUS Presidential Young Professorship grant (A-0009982-00-00) and the MOE AcRF Tier 1 24-1234-P0001 Funding. The authors would like to thank the PranaLab for their generous support and for providing the collaborative environment necessary to conduct this research. We also thank the support from Swiss AI Initiative Small Grant, NVIDIA Academic Grant, and Google Research Funding.

References

- [1] Yinoussa Adegolodjo, Laurent Goffin, Michel De Mathelin, and Hadrien Courte-cuisse. 2019. Robotic Insertion of Flexible Needle in Deformable Structures Using Inverse Finite-Element Simulation. *IEEE Transactions on Robotics* 35, 3 (2019), 697–708. doi:10.1109/TRO.2019.2897858
- [2] Atilim Gunes Baydin, Barak A Pearlmutter, Alexey Andreyevich Radul, and Jeffrey Mark Siskind. 2018. Automatic differentiation in machine learning: a survey. *Journal of machine learning research* 18, 153 (2018), 1–43.
- [3] Sofien Bouaziz, Sebastian Martin, Tiantian Liu, Ladislav Kavan, and Mark Pauly. 2023. Projective dynamics: Fusing constraint projections for fast simulation. In *Seminal Graphics Papers: Pushing the Boundaries, Volume 2*. 787–797.
- [4] E. Coevoet, T. Morales-Bieze, F. Largilliere, Z. Zhang, M. Thieffry, M. Sanz-Lopez, B. Carrez, D. Marchal, O. Goury, J. Dequidt, and C. Duriez. 2017. Software toolkit for modeling, simulation, and control of soft robots. *Advanced Robotics* 31, 22 (Nov. 2017), 1208–1224. doi:10.1080/01691864.2017.1395362 Publisher: Taylor & Francis.
- [5] Jonas Degraeve, Michiel Hermans, Joni Dambre, and Francis Wyffels. 2019. A differentiable physics engine for deep learning in robotics. *Frontiers in neurorobotics* 13 (2019), 6.
- [6] Tao Du, Kui Wu, Pingchuan Ma, Sebastien Wah, Andrew Spielberg, Daniela Rus, and Wojciech Matusik. 2021. Diffpd: Differentiable projective dynamics. *ACM Transactions on Graphics (ToG)* 41, 2 (2021), 1–21.
- [7] Kenny Erleben. 2018. Methodology for Assessing Mesh-Based Contact Point Methods. *ACM Trans. Graph.* 37, 3 (June 2018), 1–30. doi:10.1145/3096239

- [8] Moritz Geilinger, David Hahn, Jonas Zehnder, Moritz Bächer, Bernhard Thomaszewski, and Stelian Coros. 2020. Add: Analytically differentiable dynamics for multi-body systems with frictional contact. *ACM Transactions on Graphics (TOG)* 39, 6 (2020), 1–15.
- [9] Eric Heiden, David Millard, Erwin Coumans, and Gaurav S Sukhatme. 2020. Augmenting differentiable simulators with neural networks to close the sim2real gap. *arXiv preprint arXiv:2007.06045* (2020).
- [10] Eric Heiden, David Millard, Hejia Zhang, and Gaurav S Sukhatme. 2019. Interactive differentiable simulation. *arXiv preprint arXiv:1905.10706* (2019).
- [11] Philipp Holl, Vladlen Koltun, and Nils Thuerey. 2020. Learning to control pdes with differentiable physics. *arXiv preprint arXiv:2001.07457* (2020).
- [12] Yuanming Hu, Luke Anderson, Tzu-Mao Li, Qi Sun, Nathan Carr, Jonathan Ragan-Kelley, and Frédo Durand. 2019. DiffTaichi: Differentiable programming for physical simulation. *arXiv preprint arXiv:1910.00935* (2019).
- [13] Krishna Murthy Jatavallabhula, Miles Macklin, Florian Golemo, Vikram Voleti, Linda Petrinì, Martin Weiss, Breandan Considine, Jérôme Parent-Lévesque, Kevin Xie, Kenny Erleben, et al. 2021. gradsim: Differentiable simulation for system identification and visuomotor control. *arXiv preprint arXiv:2104.02646* (2021).
- [14] Quentin Le Lidec, Igor Kalevatykh, Ivan Laptev, Cordelia Schmid, and Justin Carpentier. 2021. Differentiable simulation for physical system identification. *IEEE Robotics and Automation Letters* 6, 2 (2021), 3413–3420.
- [15] Yifei Li, Tao Du, Kui Wu, Jie Xu, and Wojciech Matusik. 2022. Diffcloth: Differentiable cloth simulation with dry frictional contact. *ACM Transactions on Graphics (TOG)* 42, 1 (2022), 1–20.
- [16] Junbang Liang, Ming Lin, and Vladlen Koltun. 2019. Differentiable cloth simulation for inverse problems. *Advances in neural information processing systems* 32 (2019).
- [17] Jun Lv, Yunhai Feng, Cheng Zhang, Shuang Zhao, Lin Shao, and Cewu Lu. 2025. Sam-rl: Sensing-aware model-based reinforcement learning via differentiable physics-based simulation and rendering. *The International Journal of Robotics Research* 44, 10–11 (2025), 1767–1783.
- [18] Miles Macklin. 2024. Warp: Differentiable Spatial Computing for Python. In *ACM SIGGRAPH 2024 Courses*. 1–147.
- [19] Miles Macklin, Kenny Erleben, Matthias Müller, Nuttapon Chentanez, Stefan Jeschke, and Viktor Makoviychuk. 2019. Non-smooth newton methods for deformable multi-body dynamics. *ACM Transactions on Graphics (TOG)* 38, 5 (2019), 1–20.
- [20] Miles Macklin, Matthias Müller, and Nuttapon Chentanez. 2016. XPBD: position-based simulation of compliant constrained dynamics. In *Proceedings of the 9th International Conference on Motion in Games*. 49–54.
- [21] Sebastian Martin, Bernhard Thomaszewski, Eitan Grinspun, and Markus Gross. 2011. Example-based elastic materials. In *ACM SIGGRAPH 2011 papers*. 1–8.
- [22] Etienne Ménager, Louis Montaut, Quentin Le Lidec, and Justin Carpentier. 2025. Differentiable Simulation of Soft Robots with Frictional Contacts. In *2025 IEEE 8th International Conference on Soft Robotics (RoboSoft)*. IEEE, 1–8.
- [23] Etienne Ménager, Louis Montaut, Quentin Le Lidec, and Justin Carpentier. 2025. Differentiable Simulation of Soft Robots with Frictional Contacts. In *2025 IEEE 8th International Conference on Soft Robotics (RoboSoft)*. 1–8. doi:10.1109/RoboSoft63089.2025.11020844
- [24] Rhys Newbury, Jack Collins, Kerry He, Jiahe Pan, Ingmar Posner, David Howard, and Akansel Cosgun. 2024. A review of differentiable simulators. *IEEE Access* (2024).
- [25] Matthew Overby, George E. Brown, Jie Li, and Rahul Narain. 2017. ADMM Projective Dynamics: Fast Simulation of Hyperelastic Models with Dynamic Constraints. *IEEE Transactions on Visualization and Computer Graphics* 23, 10 (Oct. 2017), 2222–2234. doi:10.1109/TVCG.2017.2730875
- [26] Tao Pang and Russ Tedrake. 2021. A convex quasistatic time-stepping scheme for rigid multibody systems with contact and friction. In *2021 IEEE International Conference on Robotics and Automation (ICRA)*. IEEE, 6614–6620.
- [27] Adam Paszke, Sam Gross, Francisco Massa, Adam Lerer, James Bradbury, Gregory Chanan, Trevor Killeen, Zeming Lin, Natalia Gimelshein, Luca Antiga, et al. 2019. Pytorch: An imperative style, high-performance deep learning library. *Advances in neural information processing systems* 32 (2019).
- [28] Yi-Ling Qiao, Junbang Liang, Vladlen Koltun, and Ming C Lin. 2021. Efficient differentiable simulation of articulated bodies. In *International Conference on Machine Learning*. PMLR, 8661–8671.
- [29] Samuel Schoenholz and Ekin Dogus Cubuk. 2020. Jax md: a framework for differentiable physics. *Advances in Neural Information Processing Systems* 33 (2020), 11428–11441.
- [30] Changkyu Song and Abdeslam Boularias. 2020. Learning to slide unknown objects with differentiable physics simulations. *arXiv preprint arXiv:2005.05456* (2020).
- [31] Tuur Stuyck and Hsiao-yu Chen. 2023. Diffxpbd: Differentiable position-based simulation of compliant constraint dynamics. *Proceedings of the ACM on Computer Graphics and Interactive Techniques* 6, 3 (2023), 1–14.
- [32] Dylan Turpin, Liqun Wang, Eric Heiden, Yun-Chun Chen, Miles Macklin, Stavros Tsogkas, Sven Dickinson, and Animesh Garg. 2022. Grasp’d: Differentiable contact-rich grasp synthesis for multi-fingered hands. In *European Conference on Computer Vision*. Springer, 201–221.
- [33] Gang Yang, Siyuan Luo, Yunhai Feng, Zhixin Sun, Chenrui Tie, and Lin Shao. 2024. Jade: A differentiable physics engine for articulated rigid bodies with intersection-free frictional contact. In *2024 IEEE International Conference on Robotics and Automation (ICRA)*. IEEE, 16915–16922.
- [34] Xinyuan Yu, Siheng Zhao, Siyuan Luo, Gang Yang, and Lin Shao. 2023. Diffclothai: Differentiable cloth simulation with intersection-free frictional contact and differentiable two-way coupling with articulated rigid bodies. In *2023 IEEE/RSJ International Conference on Intelligent Robots and Systems (IROS)*. IEEE, 400–407.
- [35] Ziqiu Zeng, Siyuan Luo, Fan Shi, and Zhongkai Zhang. 2025. Fast But Accurate: A Real-Time Hyperelastic Simulator with Robust Frictional Contact. 44, 4, Article 88 (July 2025), 19 pages. doi:10.1145/3730834
- [36] Yaofeng Desmond Zhong, Jiequn Han, and Georgia Olympia Briki. 2022. Differentiable physics simulations with contacts: Do they have correct gradients wrt position, velocity and control? *arXiv preprint arXiv:2207.05060* (2022).
- [37] Yaofeng Desmond Zhong, Jiequn Han, Biswadip Dey, and Georgia Olympia Briki. 2023. Improving gradient computation for differentiable physics simulation with contacts. In *Learning for dynamics and control conference*. PMLR, 128–141.

A Frictional Contact

A.1 Construct Local Transformation

When both $\|\delta_f\|$ and $\|\lambda_f\|$ are nonzero, we define

$$\begin{aligned} \mathbf{R} &= \frac{1}{\|\delta_f\|} \begin{bmatrix} \|\delta_f\| & 0 & 0 \\ 0 & \delta_{f_1} & \delta_{f_2} \\ 0 & -\delta_{f_2} & \delta_{f_1} \end{bmatrix} \\ &= \frac{1}{\|\lambda_f\|} \begin{bmatrix} \|\lambda_f\| & 0 & 0 \\ 0 & -\lambda_{f_1} & -\lambda_{f_2} \\ 0 & \lambda_{f_2} & -\lambda_{f_1} \end{bmatrix}, \end{aligned} \quad (34)$$

which naturally aligns δ , λ , and their differentials in the contact-aligned basis in Equation (16). However, this nonzero assumption does not always eliminate numerical singularities. Note that $|\delta_f|$ can be near zero under static friction, and $|\lambda_f|$ can be near zero under separation. Although our smooth formulation keeps these quantities nominally nonzero, finite-precision round-off can still drive them effectively to zero, leading to ill-conditioned normalization and unstable matrix assembly.

So in practice, we define a threshold $\tau \ll 1$. As long as at least one of $\|\delta_f\|$ and $\|\lambda_f\|$ is larger than τ , we just use it to assemble \mathbf{R} (i.e., determine the main friction direction). If both $\|\delta_f\|$ and $\|\lambda_f\|$ are less than τ , it means current contact is nearly symmetric under rotation along normal direction; so we just choose $\mathbf{R} = \mathbf{I}$.

A.2 Impact of Smoothing on Forward Simulation

To verify that the smoothing introduced in the Fischer-Burmeister (FB) formulation has a negligible impact on forward simulation accuracy, we conduct a simple yet effective experiment inspired by the friction test in [35]. Specifically, we apply a constant horizontal force of magnitude 0.1 mg to two sliding blocks with slightly different friction coefficients. The friction coefficients μ are set to 0.101 and 0.099, respectively, and the smoothing parameter is chosen as $2\epsilon^2 = 10^{-6}$.

Under this setting, the block with friction coefficient $\mu = 0.101$ successfully remains stationary, corresponding to the static friction regime, while the block with friction coefficient $\mu = 0.099$ gradually begins to slide, indicating a transition to kinetic friction. This experiment in Figure 14 demonstrates that, despite the introduced smoothness, the FB formulation preserves the accuracy of forward frictional behavior up to a precision of 10^{-3} , which is consistent with

the accuracy reported in [35]. These results confirm that the smoothing primarily facilitates differentiation while having a negligible effect on the fidelity of the forward simulation.



Fig. 14. Friction behavior at time step 0 (left) and 3000 (right): blue block with $\mu = 0.101$ and red block with $\mu = 0.099$

B Local Projection Differentiation

B.1 Construction of \mathbf{D} and \mathbf{T} , 2D formulation

In the main text, we have defined auxiliary matrices: $\mathbf{D}\mathbf{x} = \text{vec}(\text{Diag}(\mathbf{x}))$ and $\mathbf{T}\text{vec}(\mathbf{X}) = \text{vec}(\mathbf{X}^\top)$, whose exact values are

$$\mathbf{D} = \begin{bmatrix} 1 & 0 & 0 \\ 0 & 0 & 0 \\ 0 & 0 & 0 \\ 0 & 0 & 0 \\ 0 & 1 & 0 \\ 0 & 0 & 0 \\ 0 & 0 & 0 \\ 0 & 0 & 0 \\ 0 & 0 & 0 \\ 0 & 0 & 1 \end{bmatrix}, \mathbf{T} = \begin{bmatrix} 1 & 0 & 0 & 0 & 0 & 0 & 0 & 0 & 0 & 0 \\ 0 & 0 & 0 & 1 & 0 & 0 & 0 & 0 & 0 & 0 \\ 0 & 0 & 0 & 0 & 0 & 0 & 0 & 0 & 1 & 0 \\ 0 & 1 & 0 & 0 & 0 & 0 & 0 & 0 & 0 & 0 \\ 0 & 0 & 0 & 0 & 1 & 0 & 0 & 0 & 0 & 0 \\ 0 & 0 & 0 & 0 & 0 & 0 & 0 & 0 & 1 & 0 \\ 0 & 0 & 1 & 0 & 0 & 0 & 0 & 0 & 0 & 0 \\ 0 & 0 & 0 & 0 & 0 & 0 & 1 & 0 & 0 & 0 \\ 0 & 0 & 0 & 0 & 0 & 0 & 0 & 1 & 0 & 0 \\ 0 & 0 & 0 & 0 & 0 & 0 & 0 & 0 & 0 & 1 \end{bmatrix}, \quad (35)$$

for 3D formulation and

$$\mathbf{D} = \begin{bmatrix} 1 & 0 \\ 0 & 0 \\ 0 & 0 \\ 0 & 1 \end{bmatrix}, \mathbf{T} = \begin{bmatrix} 1 & 0 & 0 & 0 \\ 0 & 0 & 1 & 0 \\ 0 & 1 & 0 & 0 \\ 0 & 0 & 0 & 1 \end{bmatrix}, \quad (36)$$

for 2D formulation

With these, when we consider the deformation energy in triangular base, previous derivation for 3D in main text still holds only by changing matrix dimensions. Now the displacement matrix $\mathbf{D}_s = [\mathbf{x}_1 - \mathbf{x}_0, \mathbf{x}_2 - \mathbf{x}_0]$ is not square, and the deformation gradient $\mathbf{F} = \mathbf{D}_s \mathbf{D}_m^{-1}$ becomes 2-rank. So in order to maintain positive singular values, we adopt thin SVD that $\mathbf{U}, \mathbf{V} \in \mathbb{R}^{3 \times 2}$ and $\boldsymbol{\sigma} \in \mathbb{R}^2$. Other formulas keep the same.

B.2 Construction of $\mathbf{W} = \frac{\partial \boldsymbol{\theta}}{\partial \boldsymbol{\sigma}}$

In the main text, we have defined the derivative matrix of singular values $\mathbf{W} = \frac{\partial \boldsymbol{\theta}}{\partial \boldsymbol{\sigma}}$, which captures the property of different constitutive-law elastic model. In this work, we respectively consider As-Rigid-As-Possible (ARAP) model and Neo-Hookean model.

ARAP. This model only keeps rotation information in SVD by setting $\boldsymbol{\theta}(\boldsymbol{\sigma}) = [1, 1, 1]^\top$, so we directly have $\mathbf{W} = \mathbf{0}$ and $M_{ij} = N_{ij} = \frac{1}{\sigma_i + \sigma_j}$.

Neo-Hookean. In this model, $\boldsymbol{\theta}$ is the minimizer of $\Psi(\boldsymbol{\theta}, \boldsymbol{\sigma}) = \frac{w}{2} \|\boldsymbol{\theta} - \boldsymbol{\sigma}\|_F^2 + \zeta(\boldsymbol{\theta})$:

$$\zeta(\boldsymbol{\theta}) = \frac{1}{2} \mu (I_1 - \log I_3 - 3) + \frac{1}{8} \lambda (\log I_3)^2 \quad (37)$$

where $I_1 = \theta_1^2 + \theta_2^2 + \theta_3^2$, $I_3 = J^2$, $J = \theta_1 \theta_2 \theta_3$, μ denotes Shear modulus and λ denotes Lamé's first parameter. By definition, we have $w = 2\mu$. Since $\boldsymbol{\theta}$ minimizes $\Psi(\boldsymbol{\theta}, \boldsymbol{\sigma})$, we have:

$$\mathbf{g} \equiv \frac{\partial \Psi}{\partial \boldsymbol{\theta}} = w(\boldsymbol{\theta} - \boldsymbol{\sigma}) + \mu(\boldsymbol{\theta} - \boldsymbol{\theta}^{-1}) + \lambda \log J \boldsymbol{\theta}^{-1} = \mathbf{0} \quad (38)$$

$$\frac{\partial \mathbf{g}}{\partial \boldsymbol{\sigma}} = -2\mu \mathbf{I}, \quad \frac{\partial \mathbf{g}}{\partial \boldsymbol{\theta}} = \underbrace{(3\mu \mathbf{I} + (\mu - \lambda \log J) \boldsymbol{\Theta}^{-2} + \lambda \boldsymbol{\theta}^{-1} \boldsymbol{\theta}^{-\top})}_{\mathbf{D}} \quad (39)$$

$$\mathbf{W} = \frac{\partial \boldsymbol{\theta}}{\partial \boldsymbol{\sigma}} = -\left(\frac{\partial \mathbf{g}}{\partial \boldsymbol{\theta}}\right)^{-1} \frac{\partial \mathbf{g}}{\partial \boldsymbol{\sigma}} = 2\mu \mathbf{D}^{-1} \left(\mathbf{I} - \frac{\lambda \boldsymbol{\theta}^{-1} \boldsymbol{\theta}^{-\top}}{1 + \lambda \boldsymbol{\theta}^{-\top} \mathbf{D}^{-1} \boldsymbol{\theta}^{-1}} \mathbf{D}^{-\top} \right) \quad (40)$$

B.3 Differentiation of Elastic Parameters

Before calculating the gradient with respect to Young's modulus E and Poisson's ratio ν , we first consider Shear modulus μ and Lamé's first parameter λ as the bridge:

$$\mu = \frac{E}{2(1+\nu)}, \quad \lambda = \frac{E\nu}{(1+\nu)(1-2\nu)}. \quad (41)$$

For hyperelastic materials, it's necessary to calculate $\frac{\partial p_i}{\partial \mu}$ and $\frac{\partial p_i}{\partial \lambda}$ when local projection is influenced by μ and λ .

In Neo-Hookean (with $w = 2\mu$) model:

$$\mathbf{g} = \mu(3\boldsymbol{\theta} - 2\boldsymbol{\sigma} - \boldsymbol{\theta}^{-1}) + \lambda \log J \boldsymbol{\theta}^{-1} = \mathbf{0} \quad (42)$$

$$\frac{\partial \mathbf{g}}{\partial \mu} = 3\boldsymbol{\theta} - 2\boldsymbol{\sigma} - \boldsymbol{\theta}^{-1}, \quad \frac{\partial \mathbf{g}}{\partial \lambda} = \log J \boldsymbol{\theta}^{-1} \quad (43)$$

$$\begin{aligned} \frac{\partial \boldsymbol{\theta}}{\partial \mu} &= -\left(\frac{\partial \mathbf{g}}{\partial \boldsymbol{\theta}}\right)^{-1} \frac{\partial \mathbf{g}}{\partial \mu} \\ &= -\mathbf{D}^{-1} \left(\mathbf{I} - \frac{\lambda \boldsymbol{\theta}^{-1} \boldsymbol{\theta}^{-\top}}{1 + \lambda \boldsymbol{\theta}^{-\top} \mathbf{D}^{-1} \boldsymbol{\theta}^{-1}} \mathbf{D}^{-\top} \right) (3\boldsymbol{\theta} - 2\boldsymbol{\sigma} - \boldsymbol{\theta}^{-1}) \end{aligned} \quad (44)$$

$$\begin{aligned} \frac{\partial \boldsymbol{\theta}}{\partial \lambda} &= -\left(\frac{\partial \mathbf{g}}{\partial \boldsymbol{\theta}}\right)^{-1} \frac{\partial \mathbf{g}}{\partial \lambda} \\ &= -\mathbf{D}^{-1} \left(\mathbf{I} - \frac{\lambda \boldsymbol{\theta}^{-1} \boldsymbol{\theta}^{-\top}}{1 + \lambda \boldsymbol{\theta}^{-\top} \mathbf{D}^{-1} \boldsymbol{\theta}^{-1}} \mathbf{D}^{-\top} \right) (\log J \boldsymbol{\theta}^{-1}). \end{aligned}$$

Then

$$\begin{aligned} \frac{\partial \text{vec}(\mathbf{P})}{\partial \mu} &= (\mathbf{V} \otimes \mathbf{U}) \mathbf{D} \frac{\partial \boldsymbol{\theta}}{\partial \mu} \\ \frac{\partial \text{vec}(\mathbf{P})}{\partial \lambda} &= (\mathbf{V} \otimes \mathbf{U}) \mathbf{D} \frac{\partial \boldsymbol{\theta}}{\partial \lambda} \end{aligned} \quad (45)$$

$$\begin{aligned} \frac{\partial \mathbf{P}}{\partial \mu} &= \mathbf{U} \text{Diag} \left(\frac{\partial \boldsymbol{\theta}}{\partial \mu} \right) \mathbf{V}^\top \\ \frac{\partial \mathbf{P}}{\partial \lambda} &= \mathbf{U} \text{Diag} \left(\frac{\partial \boldsymbol{\theta}}{\partial \lambda} \right) \mathbf{V}^\top. \end{aligned} \quad (46)$$

After differentiation, we have

$$\begin{aligned} \mathcal{K}_\mu &= h^2 \sum_i 2G_i^\top \left(\mu_i \frac{\partial p_i}{\partial \mu_i} + \mathbf{p}_i - G_i \mathbf{q} \right) \\ \mathcal{K}_\lambda &= h^2 \sum_i 2G_i^\top \left(\mu_i \frac{\partial p_i}{\partial \lambda_i} \right), \end{aligned} \quad (47)$$

and

$$\begin{aligned}\frac{\partial L}{\partial \mu} &= \mathbf{z}^\top \mathcal{K}_\mu, & \frac{\partial L}{\partial \lambda} &= \mathbf{z}^\top \mathcal{K}_\lambda \\ \frac{\partial L}{\partial E} &= \frac{\partial L}{\partial \mu} \frac{\partial \mu}{\partial E} + \frac{\partial L}{\partial \lambda} \frac{\partial \lambda}{\partial E} \\ \frac{\partial L}{\partial v} &= \frac{\partial L}{\partial \mu} \frac{\partial \mu}{\partial v} + \frac{\partial L}{\partial \lambda} \frac{\partial \lambda}{\partial v}.\end{aligned}\quad (48)$$

B.4 Degeneracy Analysis

In main text, we have assumed the non-degeneracy of Σ , which is not always true. When degeneracy exists, i.e. $\sigma_i = \sigma_j$, $d\mathbf{U}$ and $d\mathbf{V}$ in current results will blow up. This comes from the fact that Σ , \mathbf{U} and \mathbf{V} are no longer deterministic functions of \mathbf{F} and the derivatives are not well-defined either. If forcing to differentiate them in the neighborhood, we need to consider the off-diagonal terms in $d\Sigma$, which are on longer zero and symmetric. Diagnosing it requires a finite rotation in the degenerate space which can not be absorbed into the infinitesimal $d\mathbf{U}$ and $d\mathbf{V}$. However, although previous derivation by assuming non-degeneracy is not rigorous and the final gradient has singularities, its limitation is well-defined when $\boldsymbol{\theta}(\boldsymbol{\sigma})$ satisfy some conditions.

We first analyze the source of singularity $\frac{\theta_i - \theta_j}{\sigma_i - \sigma_j}$ which comes from the degeneracy $\sigma_i = \sigma_j$. Do first-order expansion around the degenerate point, $\boldsymbol{\sigma} = \bar{\boldsymbol{\sigma}} + \mathbf{h}$ and $\boldsymbol{\theta} = \boldsymbol{\theta}(\bar{\boldsymbol{\sigma}}) + \mathbf{W}\mathbf{h}$, and denote $\mathbf{h} = t\mathbf{v}$:

$$\lim_{t \rightarrow 0} \frac{\theta_i - \theta_j}{\sigma_i - \sigma_j} = \frac{(W_{i:} - W_{j:})\mathbf{v}}{v_i - v_j}.\quad (49)$$

This limitation depends on the path direction \mathbf{v} in general, which makes $\frac{\partial \text{vec}(\mathbf{P})}{\partial \text{vec}(\mathbf{F})}$ not well-defined. It is path-independent if and only if $W_{i:} - W_{j:} = \alpha(\mathbf{e}_i^\top - \mathbf{e}_j^\top)$, so that the limitation becomes α . Denote $I(\bar{\boldsymbol{\sigma}})$ as the degenerate block at $\bar{\boldsymbol{\sigma}}$, which means $\forall \Pi \in S_I : \Pi \bar{\boldsymbol{\sigma}} = \bar{\boldsymbol{\sigma}}$, where S_I is the symmetric group (permutation group) on I . The condition can be written as

$$\begin{aligned}\forall \Pi \in S_I : \mathbf{W}_{II}(\bar{\boldsymbol{\sigma}})\Pi &= \Pi \mathbf{W}_{II}(\bar{\boldsymbol{\sigma}}) \\ \Leftrightarrow \mathbf{W}_{II}(\bar{\boldsymbol{\sigma}}) &= \alpha \mathbf{I} + \beta \mathbf{1}\mathbf{1}^\top,\end{aligned}\quad (50)$$

and is called within-block commutation.

Moreover, the $\mathbf{P}(\mathbf{F})$ itself must be well-defined with degeneracy, requiring that $\boldsymbol{\theta}(\boldsymbol{\sigma})$ preserves degeneracy, $\forall \Pi \in S_I : \boldsymbol{\theta}(\bar{\boldsymbol{\sigma}}) = \Pi \boldsymbol{\theta}(\bar{\boldsymbol{\sigma}})$. Otherwise $\mathbf{P} = \mathbf{U}\boldsymbol{\Theta}\mathbf{V}^\top$ will depend on the gauge selection (the arbitrary rotation in degenerate space). So combining Eq. 50, the whole sufficient and necessary condition for $\mathbf{P}(\mathbf{F})$'s Fréchet differentiability is

$$\forall \Pi \in S_I, \exists U \ni \bar{\boldsymbol{\sigma}} : \boldsymbol{\theta}(\Pi\boldsymbol{\sigma}) = \Pi\boldsymbol{\theta}(\boldsymbol{\sigma}), \forall \boldsymbol{\sigma} \in U,\quad (51)$$

which is called local equivariance near the degenerate point $\bar{\boldsymbol{\sigma}}$.

As for the elastic models of our interest, $\boldsymbol{\theta}(\boldsymbol{\sigma})$ is the **unique** minimizer of $\Psi(\boldsymbol{\theta}, \boldsymbol{\sigma}) = \frac{\nu}{2} \|\boldsymbol{\theta} - \boldsymbol{\sigma}\|_F^2 + \zeta(\boldsymbol{\theta})$. Since our models focus on the **isotropic** elasticity, $\forall \Pi \in S_n : \zeta(\boldsymbol{\theta}) = \zeta(\Pi\boldsymbol{\theta})$ and $\|\boldsymbol{\theta} - \boldsymbol{\sigma}\|_F^2 = \|\Pi\boldsymbol{\theta} - \Pi\boldsymbol{\sigma}\|_F^2$ (here the subscript means norm kernel which is identity for isotropic L2 norm), and hence $\Psi(\boldsymbol{\theta}, \boldsymbol{\sigma}) = \Psi(\Pi\boldsymbol{\theta}, \Pi\boldsymbol{\sigma})$. Since $\boldsymbol{\theta}(\Pi\boldsymbol{\sigma})$ minimizes $\Psi(\boldsymbol{\theta}, \Pi\boldsymbol{\sigma})$, it also minimizes $\Psi(\Pi^{-1}\boldsymbol{\theta}, \boldsymbol{\sigma})$ and equals to $\Pi\boldsymbol{\theta}(\boldsymbol{\sigma})$. Eq. 51 holds globally, then of course $\mathbf{P}(\mathbf{F})$ is

Fréchet differentiable and at degenerate point $\sigma_i = \sigma_j$, we have

$$\begin{aligned}M_{ij} &= \frac{1}{2} \left(W_{ii} - W_{ij} + \frac{\theta}{\sigma} \right) \\ N_{ij} &= \frac{1}{2} \left(W_{ii} - W_{ij} - \frac{\theta}{\sigma} \right).\end{aligned}\quad (52)$$